

**DESIGN OF PLASMONIC NANOSTRUCTURES FOR SINGLE MOLECULE
DETECTION BASED ON FLUORESCENCE DEPENDENT SURFACE
PLASMON COUPLED EMISSION**

by

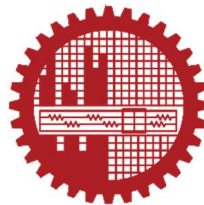
Md. Mukhlasur Rahman Tanvir

A thesis submitted in partial fulfillment of the requirements for the degree of

Master of Science

in the

Department of Electrical and Electronic Engineering
Bangladesh University of Engineering and Technology



August, 2018

Declaration

It is hereby declared that this thesis or any part of it has not been submitted elsewhere for the award of any degree or diploma.

(Md. Mukhlasur Rahman Tanvir)

Student ID: 1015062215 P

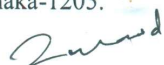
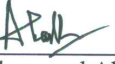
Dedication

Dedicated to my loving parents.

Approval Certificate

The thesis titled “DESIGN OF PLASMONIC NANOSTRUCTURES FOR SINGLE MOLECULE DETECTION BASED ON FLUORESCENCE DEPENDENT SURFACE PLASMON COUPLED EMISSION” submitted by Md. Mukhlasur Rahman Tanvir, Student ID: 1015062215 P, Session: October 2015 has been accepted as satisfactory in partial fulfillment of the requirement for the degree of MASTER OF SCIENCE IN ELECTRICAL AND ELECTRONIC ENGINEERING on August 13, 2018.

Board of Examiners

1. 
_____ Chairman (Supervisor)
Dr. Md. Kawsar Alam
Associate Professor
Department of EEE, BUET
Dhaka-1205.
2. 
_____ Member (Ex-Officio)
Dr. Md. Shafiqul Islam
Professor and Head
Department of EEE, BUET
Dhaka-1205.
3. 
_____ Member
Dr. Samia Subrina
Professor
Department of EEE, BUET
Dhaka-1205.
4. 
_____ Member
Dr. Md Zunaid Baten
Assistant Professor
Department of EEE, BUET
Dhaka-1205.
5. 
_____ Member (External)
Dr. Mohammed Abdul Basith
Professor
Department of Physics, BUET
Dhaka-1205.

Abstract

Surface plasmon-coupled emission (SPCE) is the complementary phenomenon of surface plasmon resonance (SPR), where the light emitted from a fluorescent molecule couples into the adjacent thin metal layer resulting in highly directional emission in the SPR angle. In addition to the high directionality of emission, SPCE has the added advantage of surface selectivity, high spectral and spatial resolution. This effect can be exploited in bioassays with high signal to noise ratio. However, SPCE based detection is still not used to image single molecule due to large detection volume, which results in low resolution imaging.

Single molecule detection requires much smaller detection volume than that is provided by typical SPCE based structure. This thesis mainly focuses on designing nanostructures to address this issue. In this work, we propose a new structure that replaces the thin metal layer – used in typical SPCE design – with a nanostructured metal layer, which contains periodic nanoholes. We use finite difference time domain (FDTD) analysis to solve Maxwell's equations and calculate detection volume, excitation field intensity, coupled power to detection side, and peak SPCE intensity for different sizes of nanoholes with varying periodicity. We use particle swarm algorithm to find the optimum combination of periodicity and diameter of the nanoholes so that the proposed structure provides minimum detection volume. Our proposed structure not only reduces the detection volume by 84 percent but also significantly improves the excitation field intensity, coupled power to detection side, and peak SPCE intensity.

Acknowledgement

I would like to thank my supervisor Dr. Md. Kawsar Alam for his continuous support and guidance. He has been super helpful and easily accessible. I still remember the night before I submit my thesis proposal. He reviewed and edited my proposal several times till late night, until it was finalized.

I also like to express my gratitude to the department of Electrical and Electronic Engineering for allowing me to use Nanoelectronic Devices and Materials Research Laboratory – 24 hours, 7 days – to carry out my time-consuming simulations.

My heartfelt thanks goes to all the members of the board of examiners for their comments, reviews, and suggestions.

Finally, I also thank my parents for always supporting me and believing in me. They inspired me whenever I felt lost in this deep dark world.

Table of Contents

| | |
|---|-----|
| Declaration | ii |
| Dedication | iii |
| Approval Certificate | iv |
| Abstract | v |
| Acknowledgement | vi |
| Table of Contents | vii |
| List of Figures | x |
| List of Tables | xiv |
| 1 Introduction..... | 1 |
| 1.1 Overview of Current Development..... | 1 |
| 1.2 Applications and Future of SPCE | 3 |
| 1.3 Drawbacks..... | 5 |
| 1.4 Thesis Structure..... | 5 |
| 2 Theoretical Overview..... | 6 |
| 2.1 Fluorophore and Fluorescence | 6 |
| 2.1.1 Quantum Yield..... | 7 |
| 2.1.2 Lifetime..... | 7 |
| 2.1.3 Fluorescence Anisotropy | 8 |
| 2.1.4 Photobleaching..... | 8 |
| 2.2 Experimental Setup | 8 |
| 2.3 Properties of SPCE..... | 10 |
| 2.3.1 Directed Emission..... | 11 |
| 2.3.2 Sample Layer Thickness..... | 11 |
| 2.3.3 Polarization | 12 |

| | | |
|-------|---|----|
| 2.3.4 | Fluorophore Position..... | 12 |
| 2.4 | Theory and Explanation of Properties of SPCE..... | 12 |
| 2.4.1 | Radiation from Dipole | 12 |
| 2.4.2 | Transfer Matrix Method..... | 13 |
| 2.4.3 | Fields in the Prism Side | 16 |
| 2.4.4 | Modes Present in the Structure | 17 |
| 2.4.5 | Approximate Estimation of Emission Angle | 19 |
| 2.5 | Summary | 19 |
| 3 | Simulation Method..... | 21 |
| 3.1 | Simulation Model..... | 21 |
| 3.1.1 | Material modelling..... | 22 |
| 3.1.2 | Fluorophore modelling..... | 22 |
| 3.1.3 | Simulation Dimension | 23 |
| 3.1.4 | Mesh Independence Test..... | 24 |
| 3.1.5 | Boundary Conditions | 24 |
| 3.1.6 | Farfield Calculation | 25 |
| 3.2 | Simulation Results..... | 26 |
| 3.3 | Summary | 30 |
| 4 | Single Molecule Detection with Nanostructures | 31 |
| 4.1 | Proposed Structure | 32 |
| 4.2 | Fabrication Feasibility..... | 35 |
| 4.3 | Dispersion Relation of the Proposed Structure | 35 |
| 4.4 | Penetration Depth..... | 38 |
| 4.5 | Excitation Field | 42 |
| 4.6 | Power Coupled to Detection Side | 44 |
| 4.7 | Peak SPCE Intensity..... | 46 |

| | | |
|-----|--|----|
| 4.8 | Comprehensive Performance Analysis | 47 |
| 4.9 | Theoretical Explanation | 51 |
| 5 | Conclusion and Future Works | 53 |
| 5.1 | Future Work | 54 |

List of Figures

| | |
|--|----|
| Figure 2.1: Experimental setup for SPCE with various excitation schemes..... | 9 |
| Figure 2.2: Cone shaped emission from the fluorophores in the multilayer structure creates illuminated circles in any observation plane normal to z-axis. Alternating polarization for multiple emission angles is shown with blue arrows. | 11 |
| Figure 2.3: Different electric field inside multilayer media. | 13 |
| Figure 2.4: Reflectance of the multilayer structure for different angle of incidence are shown. Sample layer thickness in (a) and (b) is 37 and 745 nm. The unbroken and dashed lines are for p and s-polarization respectively. The angles where minima of reflectance occur come with alternating polarization. | 16 |
| Figure 2.5: Confined Fabry-Perot Resonator - A dielectric layer of thickness t and refractive index ϵd inserted between two ideal metal layers. | 16 |
| Figure 2.6: θFPR with s and p-polarized emission angles for different sample layer thickness. Note at 150 nm the emission angle changes discontinuously and polarization changes abruptly. | 18 |
| Figure 3.1: Experimental emission and absorption spectrum of Rhodamine B[28]. The difference between maximum emission and extinction wavelength, called stokes shift, is around 22 nm. ... | 22 |
| Figure 3.2: Fields at symmetric and antisymmetric boundary conditions. | 25 |
| Figure 3.3: Far field radiation intensity of a vertical and horizontal dipole inside the prism projected in a hemispherical observation plane. The vertical dipole only shows p-polarized emissions where the horizontal dipole shows both p and s-polarized emission. | 27 |
| Figure 3.4: $E\theta^2$ and $E\phi^2$ horizontal dipole measured in far field. The intensity is shown in Figure 3.3b. $E\theta^2$ is maximum in the direction of p-polarized emission. $E\phi^2$ is maximum in the direction of s-polarized emission. | 28 |

Figure 3.5: Power per solid angle of a horizontal dipole seen in a plane containing the dipole moment ($\phi = 0^\circ$) and normal to the dipole moment ($\phi = 90^\circ$). 29

Figure 3.6: Electric field intensity (normalized) in various zenith angle of a horizontal dipole seen in xz plane containing the dipole moment ($\phi = 0^\circ$) and in yz plane normal to the dipole moment ($\phi = 90^\circ$). The s and p-polarized peaks occurs at interlaced angles..... 29

Figure 4.1: Structure used for SPCE generation with different excitation schemes..... 33

Figure 4.2: Metal with nanoholes. The period of the nanohole array is P and the diameter of a nanohole is d. 33

Figure 4.3: Frequency (ω) vs in-plane wavevector (β) or dispersion relation. Only the leaky modes are shown. Left and right most straight lines are light lines of air and glass, respectively. The in-plane wavevectors for typical structure and proposed structure with nanoholes – P = 520 nm and d = 170 nm – lie between the air and glass light lines. 37

Figure 4.4: Penetration depth δpd vs Period of the nanoholes. Diameter of the nanoholes is considered to be 170 nm. The penetration depth shows a steep deep, which occurs at P = 520 nm. At this point the penetration depth is only 40 nm that is very suitable for single molecule detection, whereas typical structure has a penetration depth of around 250 nm. 38

Figure 4.5: Penetration depth (δpd) vs period (P) of the nanoholes for different three different diameters of the holes. Blue triangle, black circle, and green diamond represent the graph for nanoholes diameter of 130, 170, and 210 nm, respectively. When diameter is 130 nm or 210 nm, there is no significant decrement in penetration depth. However, for a diameter of 170 nm, there is a sharp minimum at around P = 520 nm. Lowest penetration depth of 40 nm is achieved at that point. 39

Figure 4.6: Penetration depth (δpd) vs diameter of the nanoholes, d (nm) for a periodicity of P = 520 nm. This figure shows a minimum at d = 170 nm, confirming our previously found result. 40

Figure 4.7: Penetration depth (δpd) vs nanohole diameter, d (nm) for different periodicity of nanoholes. Blue triangle, black circle, and green square represent the penetration depth of the proposed structure for a periodicity of 490, 520, and 550 nm, respectively..... 41

Figure 4.8: Excitation field intensity vs periodicity of nanoholes. The excitation field intensities are normalized by corresponding excitation field intensities of the typical structure. The fields are calculated at a distance of 30 nm from the metal and sample/spacer layer interface. The diameter of the nanoholes is 170 nm. Proposed structure's performance is marked with blue circle. 42

Figure 4.9: Excitation field intensity vs diameter of nanoholes. The excitation field intensities are normalized by corresponding excitation field intensities of the typical structure. The fields are calculated at a distance of 30 nm from the metal and sample/spacer layer interface. The periodicity of the nanoholes is 520 nm. Performance of the proposed structure is marked with blue circle. 43

Figure 4.10: Power coupled to detection side as a function of periodicity of the nanoholes. Coupled power is normalized by the corresponding coupled power of the typical structure. Coupled power is calculated by integrating the far-field at a distance of 1 m that is generated by projecting near field to far field. The diameter of the nanoholes is 170 nm. Performance of the proposed structure is marked with blue circle. 44

Figure 4.11: Power coupled to detection side as a function of the diameter of the nanoholes. Coupled power is normalized by the corresponding coupled power of the typical structure. Coupled power is calculated by integrating the far-field at a distance of 1 m that is generated by projecting near field to far field. The period of the nanoholes is 520 nm. Performance of the proposed structure is marked with blue circle. 45

Figure 4.12: Peak SPCE intensity vs period of the nanoholes. The maximum emitted electric field intensity at the detection side is named as peak SPCE intensity. Peak SPCE intensity is normalized by the corresponding peak SPCE intensity of the typical structure. The diameter of the nanoholes is 170 nm. Performance of the proposed structure is marked with blue circle. 46

Figure 4.13: Peak SPCE intensity vs diameter of the nanoholes. The maximum emitted electric field intensity at the detection side is named as peak SPCE intensity. Peak SPCE intensity is normalized by the corresponding peak SPCE intensity of the typical structure. The period of the nanoholes is 520 nm. Performance of the proposed structure is marked with blue circle. 47

Figure 4.14: Bar chart of performance of proposed structure compared with typical structure. The performances are expressed in percentage of that of the typical structure. Blue bars correspond to the typical structure whereas yellow bars correspond to the proposed structure. 49

Figure 4.15: Comparison of the performances of different structures. The dark blue, light blue, green, and yellow bars represent the typical, proposed, candidate 1, and candidate 2 structure, respectively. 51

List of Tables

| | |
|---|----|
| Table 4.1: Performance comparison between typical and proposed structure..... | 48 |
| Table 4.2: Comparison of proposed structure with typical and other candidate structures | 50 |

Chapter 1

Introduction

The radiation pattern of excited fluorescent molecules change significantly if a discontinuity in refractive index as an interface is present at a distance comparable to the wavelength of the radiation [1]. The interface acts as a high Q multi-bandpass filter which radiates only at some specific angles to the other side. Usually for a dielectric-dielectric interface, the maximum emission is found in the direction of critical angle of total internal reflection. If a thin metal layer is inserted between the dielectric layers, directional emission of highly polarized light is found, which is called **surface plasmon coupled emission (SPCE)**. The emission angles are frequency sensitive and very sharp. The maximum distance at which fluorophore near field couples with the metal layer are small compared to dielectric interfaces. Also molecules very close to metal have very short lifetime and loses their energy in non-radiative transition due to quenching. They make the detection volume of SPCE axially very thin. SPCE has high potential as a microscopy or sensory scheme due to these properties. The only drawback of SPCE is that low amount energy is coupled through the metal layer to the other side of the interface. A brief discussion about the recent research regarding SPCE will allow us to understand the importance of the field and hence our motivation towards this thesis topic.

1.1 Overview of Current Development

Since SPCE was first reported by Benner *et al.*[2], it has been studied both theoretically [1], [3]–[5] and experimentally [6]–[9]. Theoretical works based on classical electromagnetic theory predicts the characteristic polarized rings of SPCE. J. Enderleins analytic approach explained single molecule fluorescence near a metal layer [4]. The study considered both well-known fluorescence quenching and reduced photo-bleaching rate. Polerecky *et al.* found explicit expressions of the angular field and intensity profile of randomly oriented dipole layer placed inside an arbitrary multilayer system [1]. Such rigorous investigation shows that, the SPCE emission angle coincides with the reflectance minimum angle. In another study, J. Enderlein *et al.* [10], theoretically proved that metal film actually reduces the sensitivity of fluorescence detection. This happens because of the loss in the metal layer. But SPCE compensates it with very narrow

spatial linewidth ($\sim 3^\circ$) and small detection volume. J.R. Lakowicz showed a new method of increasing sensitivity in detection which allows detection of fluorophores over substantial distances beyond the metal-sample interface [7]. In an investigation, I. Gryczynski *et al.* reported observation of directional surface plasmon coupled emission (SPCE) excited directly or by evanescent field [11]. They also claimed that SPCE displays unique optical properties and can be collected with an efficiency near 50%. In another study, I. Gryczynski *et al.* observed the effect of sample layer thickness and find multiple emission angles as the thickness is increased [8]. Another important finding is that the emitted light is highly polarized and altering polarization with emission angles. Other emission modes are explained as waveguide modes. N. Calander reported a theoretical approach to surface plasmon coupled emission from planar structure and compared the simulated result with experimental findings [12]. In another investigation [13], N. Calander explained waveguide modes of SPCE theoretically and also compared with the experimental results. J. Enderlein and T. Ruckstuhl presented a theoretical analysis of SPCE, studying the potential enhancement of the fluorescence collection efficiency, brightness, quantum-yield, and photo-stability [5]. Comparing the result with detection on pure glass surface, they showed that SPCE does not lead to any improvement and the metal layer reduced the sensitivity of fluorescence detection. Z. Gryczynski *et al.* explained two factors for minimizing detection volume [6]. They are the depth of evanescent excitation wave and distance dependent power coupling. Detection volume in Reverse Kretschmann configuration only depends on the coupling. In Kretschmann configuration, detection volume is the product of penetration depth of the excitation field and distance dependent coupling. Again, Z. Gryczynski *et al.* [14], proposed a new approach to fluorescence correlation spectroscopy (FCS) and single molecule detection (SMD) based on SPCE. They also claimed that collected SPCE is very sensitive to the change in fluorophore position and orientation, which opens a new possibility of studying conformational changes of macromolecules in real time.

There are a variety of possible ways of enhancing the performance of the SPCE. One possible solution is the use of better photodetector, optical system with higher numerical aperture (NA), and a highly sensitive detection system. The collection efficiency of SPCE can also be increased by using a conical mirror around the hemispherical prism so that SPCE ring is reflected into a single point [15]. This increases the intensity about 500 times.

Another way of increasing the intensity of SPCE is to modify the host environment and increase the fluorescence of the fluorophores. M. H. Chowdhury et al., reported that self-assembled monolayers of colloidal silver nanoparticles can increase the intensity of the SPCE

This scheme increases SPCE intensity 35 times by increasing fluorescence. Recently, S. Venkatesh et al., used carbon allotropes as spacer to achieve fluorescence enhancement in SPCE [16]. This benchmark setting work reported that, carbon nanodots (AgCD) increases fluorescence as much as 1000 times. They achieved the long-desired goal of 1000 times SPCE enhancement. Increasing the coupling between the prism and the sample layer also increases the intensity of SPCE.

1.2 Applications and Future of SPCE

Fluorescence-based biosensors track fluorescent labels with organic molecules like, DNA, protein, nucleic acids, lipids etc. Fluorophores are advantageous as a labelling molecule because of handling, high stability, spatial resolution, multianalyte detection, sensitivity, rapid detection, simple excitation and detection instrumentation and low total system cost with possibility of miniaturization. Fluorescence-based biosensors typically measure changes in readout modes e.g., fluorescence intensity, lifetime or polarization. This allows to observe the real time movement of that labelled organic chemical. It has improved bio-detection method and opened new opportunities in biochemistry and material science studies. In general, fluorescence is used in life science as a non-destructive way of tracking biological molecules where SPCE plays a vital role.

Current necessity for detection of very low concentrations of analytes needs improved sensitivity in fluorescence-based sensors. Although detection of single fluorescent molecules and even measurement of their orientation is possible, the detection systems are very expensive. SPCE can be an alternative simple, compact, portable and very cheap method for enhanced detection. The lowered detection volume achieved by the SPR excitation mechanism allows even lower number of molecules to be present inside the watched volume and reduces the noise in correlation spectroscopy. Dynamics of many interactions (like muscle contraction which results from interactions between actin and myosin cross-bridges) are quite different in live sample (contracting muscle than in vitro) because of the molecular crowding. In addition, each subsystem is generally in a different stage of its dynamic cycle, and so temporal measurements are time averages. To avoid complications related to crowding and averaging, it is necessary to follow time behavior of

a single subsystem (single cross-bridge in muscle). To be able to do so, it is necessary to collect data from an extremely small volume (an attoliter, 10^{-18} liter). Surface plasmon coupled emission (SPCE) provides such a volume in a live sample, and has been used for detection of single muscle fiber [17]. Muscle is fluorescently labelled and placed on a coverslip coated with a thin layer of noble metal. The laser beam is incident at a surface plasmon resonance (SPR) angle, at which it penetrates the metal layer and illuminates muscle by evanescent wave. The volume from which fluorescence emanates is a product of two near-field factors: the depth of evanescent wave excitation and a distance dependent coupling of excited fluorophores to the surface plasmons. The emission is collected for different regions of excitations, forming the image. The resulting image is higher resolution than the one formed by ordinary total internal reflection field microscopy (TIRFM).

The drastic dependence of metal layer conductivity on wavelength gives a fine spectral resolution and simultaneous detection of different analytes labelled by different fluorophores are possible. Parallel detection of spectrally different fluorophores has been done experimentally without the use of additional dispersive elements [18].

SPCE is very favorable in applications where very low-level noise is acceptable. The power coupled to the other side of the metal layer drops off exponentially, and thus only the fluorophores close to the metal layer contributes to the SPCE. Fluorophores very close to the metal layer are quenched. The power coupled by molecules whose moments are parallel to the metal plane provide very little power ($\sim 1\%$) compared to vertical moment molecules. So only very oriented molecular radiation adds to the SPCE signal. This has been demonstrated to lead to better noise performance [6]. The high directionality of fluorescence emission in SPCE may help to better discriminate between fluorescence and any other background which does not show a similar directionality in emission (potentially Rayleigh and Raman scattering).

As SPCE angles are sensitive to sample layer thickness, accurate measurement of thickness at the point of excitation may also be possible. By placing fluorophores inside the desired layer, the number and value of the SPCE can determine the created layers thickness by a technology. Using different fluorophores can be a cross checking mechanism.

1.3 Drawbacks

Despite the high potential of SPCE based detection, it has some serious drawbacks. First of all, the power coupling efficiency is very poor which leads to low intensity electric field at the detector side. Till date, fluorescence enhancement is done using AgCD, but the basic limitation of the structure about power coupling still remains [16].

A relatively larger detection volume is another issue which is not desired in super-sensitive detection schemes like single molecule detection (SMD). To use this method in single molecule detection, it is necessary to minimize the detection volume. Moreover, background noise is also another problem that degrades the signal to noise ratio (SNR) performance of the detection.

1.4 Thesis Structure

The thesis deals with designing nanostructures to provide smaller detection volume. It also tries to remove the current limitations of SPCE and solve the drawbacks. The text is divided into five chapters.

- Chapter 1 introduces to SPCE mechanism and overview of its current development.
- Chapter 2 explains fundamental properties of SPCE and also investigates different modes present in the structure while generating SPCE.
- Chapter 3 deals with the simulation method to solve Maxwell's equation and uses finite difference time domain (FDTD) method because of its versatility. It includes all the necessary modelling parameters used in the FDTD simulation. In the last part of this chapter, FDTD simulation results which confirm previously discussed properties of SPCE are also presented.
- Chapter 4 proposes a new structure to image single molecule. It also compares the performances of the new structure with that of the typical structure and other possible candidate structures. It finds the optimum structure that provides the minimum detection volume.
- Chapter 5 summarizes the key features and draws a conclusion of this thesis.

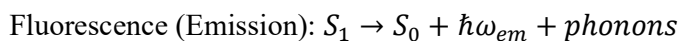
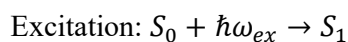
Chapter 2

Theoretical Overview

The objective of this chapter is to deliver theoretical background necessary to understand the mechanism of SPCE. Firstly, fundamental principles of fluorescence and various parameters associated with it are discussed. Then the basic experimental structure used in the experiments are described. The rest of the chapter describes experimental properties of SPCE and the necessary theory to explain it.

2.1 Fluorophore and Fluorescence

Fluorescence is the emission of light by a substance that has absorbed light or other electromagnetic radiation [19]. Fluorescent molecules, called fluorophores, absorb light at a certain frequency, called excitation frequency (w_{ex}). This elevates an orbital electron of a molecule, atom, or nanostructure from a low energy state S_0 to an excited high energy state S_1 . Fluorescence occurs when the excited electron relaxes to its ground state by emitting a photon of emission frequency (w_{em}) from the excited singlet state.



S_0 is called the ground state of the fluorophore (fluorescent molecule), and S_1 is its first (electronically) excited singlet state.

The emission and excitation frequency are different (for most cases $w_{ex} > w_{em}$) and dependent on the environment the fluorophore is on. The difference between the emission and excitation frequency is called Stokes' Shift. Large Stokes Shifts' are ideal for any fluorescence spectroscopy technique.

A fluorophore in S_1 can relax by various competing pathways. It can undergo non-radiative relaxation in which the excitation energy is dissipated as phonons to the solvent. Fluorescence

occurs in a radiative relaxation path. Various parameters can be used to quantify fluorescence, e.g. quantum yield, lifetime etc.

2.1.1 Quantum Yield

The quantum yield or quantum efficiency (Φ) can be defined as,

$$\Phi = \frac{\Gamma_f}{\sum_i \Gamma_i} = \frac{\text{Number of photons emitted}}{\text{Number of photons absorbed}}$$

where Γ_f is the rate constant of spontaneous emission of radiation and $\sum_i \Gamma_i$ is the sum of all rates of excited state decay. The maximum fluorescence quantum yield is 1, each photon absorbed results in a photon emitted. The quantum yield of a fluorophore compares the processes which return the molecule to its ground state by radiative processes to all processes (radiative and non-radiative).

2.1.2 Lifetime

The fluorescence lifetime refers to the average time the molecule stays in its excited state before emitting a photon. It is given by,

$$\tau = \left(\sum_i \Gamma_i \right)^{-1} = (\Gamma_{\text{radiative}} + \Gamma_{\text{non-radiative}})^{-1} \quad (0.1)$$

The creation of additional non-radiative paths will add rate constants in the summation and decrease the amount of time a fluorescent molecule is in its excited state. It is very sensitive to the fluorophore environment, a fact used in fluorescence lifetime spectroscopy. Fluorescence follows first order kinetics,

$$[S_1]_t = [S_1]_0 e^{-t/\tau} \quad (0.2)$$

where $[S_1]_t$ is the concentration of excited state molecules at time t , and $[S_1]_0$ is the initial concentration.

2.1.3 Fluorescence Anisotropy

Fluorophores are more likely to be excited by photons if the transition moment of the fluorophore is parallel to the electric vector of the photon. The polarization of the emitted light will also depend on the transition moment. The transition moment is dependent on the physical orientation of the fluorophore molecule. For fluorophores in solution this means that the intensity and polarization of the emitted light is dependent on rotational diffusion. Therefore, anisotropy measurements can be used to investigate how freely a fluorescent molecule moves in a particular environment. Fluorescence anisotropy can be defined quantitatively as,

$$r = \frac{I_{\parallel} - I_{\perp}}{I_{\parallel} + 2I_{\perp}} \quad (0.3)$$

where I_{\parallel} is the emitted intensity parallel to polarization of the excitation light and I_{\perp} is the emitted intensity perpendicular to the polarization of the excitation light [20].

2.1.4 Photobleaching

Photobleaching or fading is the photochemical alteration of a fluorophore molecule such that it permanently is unable to fluoresce. This is caused by cleaving of covalent bonds or non-specific reactions between the fluorophore and surrounding molecules. In microscopy, photo-bleaching may complicate the observation of fluorescent molecules, since they will eventually be destroyed by the light exposure necessary to stimulate them into fluorescing.

2.2 Experimental Setup

Basic experimental structure used to generate SPCE from fluorescent molecules is shown in Figure 2.1. A metal (silver) layer of 50 nm thickness is deposited on a hemispherical glass (SiO_2) prism. A sample layer of varying thickness is put on the metal. A glass layer (10 nm) acts as a spacer between the metal and molecules. The molecules are thought to be situated everywhere inside this sample layer except in the spacer region. A bulk material (usually Air or Water) covers all the space above the spacer layer.

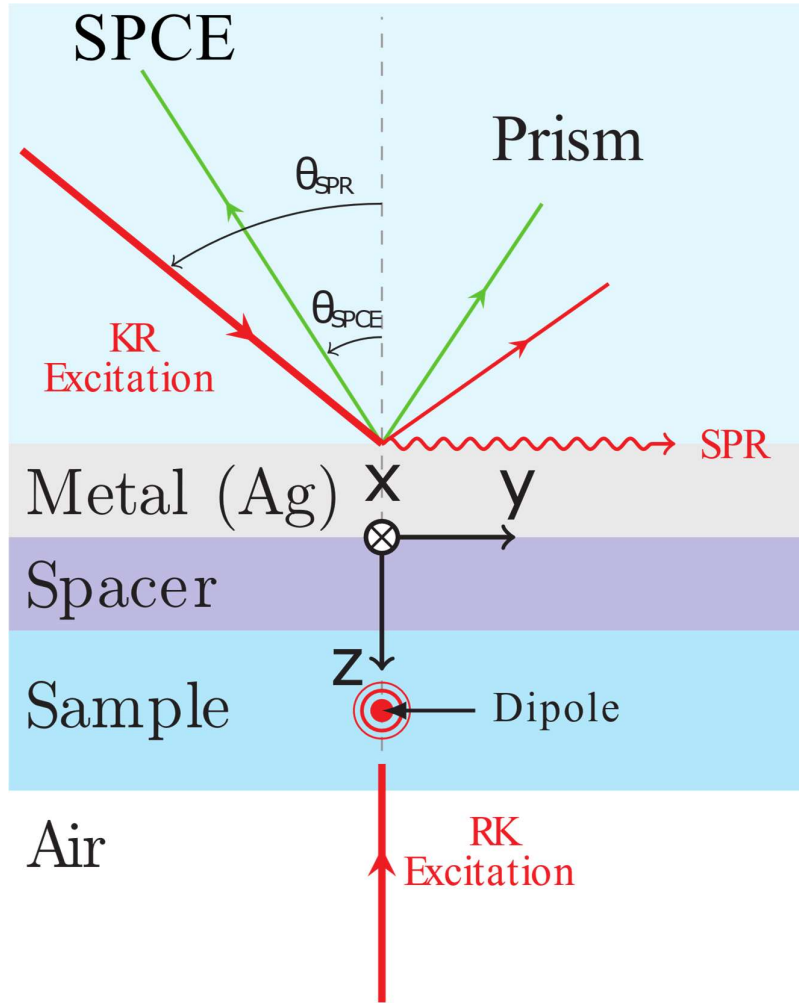


Figure 2.1: Experimental setup for SPCE with various excitation schemes.

In the experimental setup, these fluorescent elements distributed in the sample layer can be excited by two schemes [11], Kretschmann (KR) and Reverse Kretschmann (RK) configuration. The excitation schemes are shown in Figure 2.1. In RK configuration the fluorophores are excited directly from the sample layer side by shining excitation frequency light at normal incidence. In KR configuration, excitation is done from prism side. It is an attenuated total reflection mode, where light of excitation frequency (ω_{ex}) falling from the prism side at the SPR angle (θ_{SPR}) creates surface plasmon resonance (SPR) in the sample layer side. These schemes are schematically shown in Figure 2.1. The horizontal and vertical components of the evanescent field decays exponentially inside the bulk material (air or water). As light is absorbed by the surface plasmons, a reflectance minimum is found at θ_{SPR} for p-polarized light. For any of these configurations, this field excites the fluorophores and emits at its emission frequency (ω_{em}). This emission interacts with the metal layer and comes out as SPCE in an angle called the SPCE angle

(θ_{SPCE}). As SPCE is the reverse process of SPR, reflectance measured from prism side at emission frequency is minimum at θ_{SPCE} . θ_{SPR} and θ_{SPCE} are different, because they are reflectance minimum angles for excitation and emission frequency. Figure 2.1 shows the RK configuration where the excitation light is directly applied on front side. In this configuration surface plasmon resonance (SPR) is not generated by excitation. In KR configuration excitation light is applied at an angle from the prism side, which generates Surface Plasmon Resonance in the sample layer. The near field dipole radiation couples with the nearby metal layer, which re-radiates in the back side. This is the Surface Plasmon Coupled Emission (SPCE).

2.3 Properties of SPCE

In this section, we summarize the key properties observed in the experiments conducted on SPCE. Once we develop our theory, we will show that simulation of the theory produces these experimental properties.

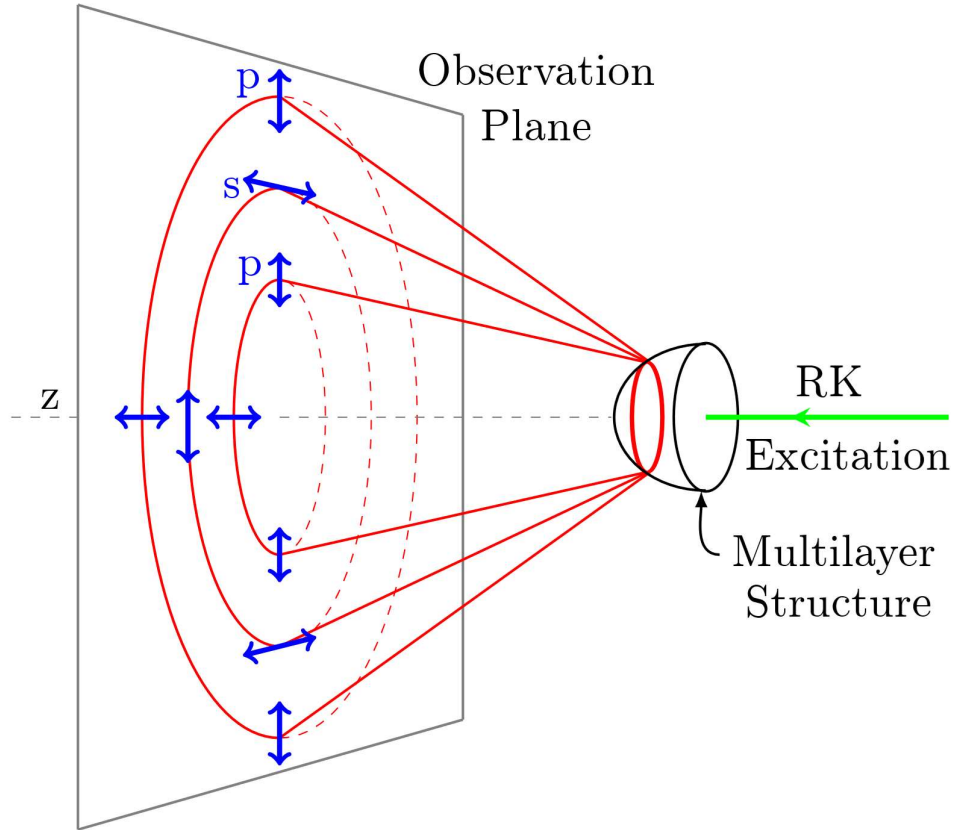


Figure 2.2: Cone shaped emission from the fluorophores in the multilayer structure creates illuminated circles in any observation plane normal to z-axis. Alternating polarization for multiple emission angles is shown with blue arrows.

2.3.1 Directed Emission

SPCE is found happen at a very specific zenith angle [21]. Emission can happen at multiple angles. The emission angle with respect to normal axis, called the SPCE angle, is shown in Figure 2.1. It is dependent on wavelength, multilayer materials and structural geometry. As illustrated in Figure 2.2, the emission has azimuthal symmetry and spreads as a cone around the z-axis. If this light is projected on a z-normal plane, it creates circular rings.

2.3.2 Sample Layer Thickness

The number of emission angles increases in a step-like fashion with the increase of sample layer thickness [8]. P-polarized emission at single angle occurs if the sample layer thickness is less than

a critical thickness. For a sample layer wider than the critical thickness, multiple rings with same center but different radius are seen on the observation plane, as illustrated in Figure 2.2.

2.3.3 Polarization

SPCE is found to be highly polarized. This is very different from the emission pattern found in using only dielectric interfaces. As it is emitted in a radial fashion, the local wavevector $\vec{k} = |\vec{k}|\vec{R}$. So the light is s-polarized if \vec{E} is in $\hat{\phi}$ direction and p-polarized if in $\hat{\theta}$ direction. For the azimuthal symmetry of the structure, the polarization of any single ring in the observation plane is same. If a ring is found to be s-polarized in one azimuthal angle, then any part of this ring contains s-polarized light. But if emission at multiple angles occur, the polarization type is interlaced between the rings. For any ring in the observation plane, the rings who have radius immediately greater or smaller than this ring has opposite polarization. The polarization scheme and interlacing is shown in Figure 2.2. To summarize, any ring has same polarization everywhere on it, but different polarization from adjacent rings. Single ring is always p-polarized.

2.3.4 Fluorophore Position

Position of fluorophore layers can be controlled in the experiment by inserting Langmuir-Blodgett films as a spacer [22]. This sheds some light into the dependence of coupled power on the distance of the layer from the metal layer. The coupled power in the prism side decays exponentially with elevation. Specimens at different height emit at same angles. Distance of fluorophores from the metal spacer layer interface has no effect on the emission angle [8].

2.4 Theory and Explanation of Properties of SPCE

2.4.1 Radiation from Dipole

We model the radiation from the fluorophores with an electrical dipole. Consider a single dipole is placed inside the sample layer. The field radiated by the dipole can be expressed as a sum of plane waves with different wavevectors \vec{k} , which is nothing but two dimensional spacial Fourier transform of the field. We will use the Weyl identity which have the following form,

$$\frac{e^{ikr}}{r} = \frac{ik}{2\pi} \int_0^{2\pi} d\phi \int_C dv \sin(v) e^{i\vec{k}\cdot\vec{r}} \quad (0.4)$$

The wavevector \vec{k} is (k, ν, ϕ) in spherical coordinates. The choice for the integration contour C is optional. The electromagnetic fields from the oscillating dipole with a dipole moment \vec{p} are given by,

$$\vec{E} = -\frac{1}{4\pi\epsilon} \nabla \times \left[\nabla \times \frac{\vec{p} e^{ikr}}{r} \right] \quad (0.5)$$

$$\vec{H} = \frac{ikc}{4\pi} \nabla \times \frac{\vec{p} e^{ikr}}{r} \quad (0.6)$$

Inserting the Weyl identity leads to,

$$\vec{E} = \frac{ik}{8\pi^2\epsilon} \int_0^{2\pi} d\phi \int_C dv \sin(v) (\vec{p} \times \vec{k}) \times \vec{k} e^{i\vec{k}\cdot\vec{r}} \quad (0.7)$$

$$\vec{H} = \frac{ik^2c}{8\pi^2} \int_0^{2\pi} d\phi \int_C dv \sin(v) \vec{p} \times \vec{k} e^{i\vec{k}\cdot\vec{r}} \quad (0.8)$$

These shows us that the electric field in free space is a summation of weighted plane waves.

The description here follows the work of [12].

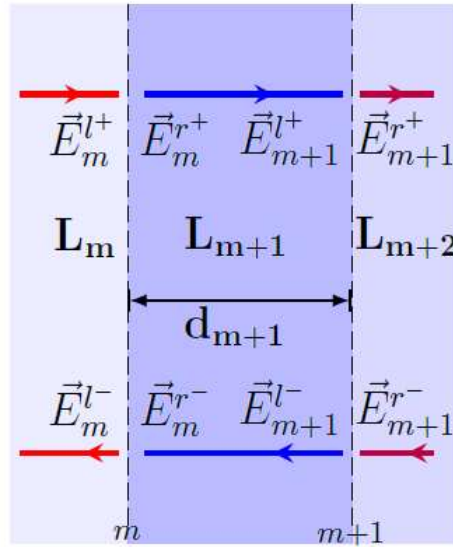


Figure 2.3: Different electric field inside multilayer media.

2.4.2 Transfer Matrix Method

Consider a plane wave incident on the multilayer structure shown in Figure 2.3 from the back side. Depending on the angle of incidence and polarization of the plane wave a portion of it will be

reflected back and some of it will be transmitted in the front side. The ratio of the intensity of transmitted and reflected light to incident light is called the transmittance (T) and reflectance (R) of a structure. For a single interface, Fresnel equations give R and T. As multiple reflection occurs in a multilayer structure, it is not straightforward to apply Fresnel equations and get R for a structure. Transfer Matrix method [23], which is presented below, can calculate R and T of a multilayer structure.

Suppose we have N ($m = 0, \dots, N - 1$) planes infinitely spread interfaces created by stacking of $N + 1$ ($L_m; m = 0, \dots, N$) layer of materials. The optical properties of this stratified media changes in the direction normal to the interfaces but has azimuthal homogeneity. Two of such interfaces with their adjacent electric field are shown in Figure 2.1. These fields are perpendicular to the wavevector \vec{k} . The subscript in the field name indicates the interface they are touching and the l or r superscript shows which side of the interface they are on, left or right. The + or - superscript corresponds to forward or backward \vec{k} . In any interface the vectors are related by,

$$\begin{bmatrix} \vec{E}_m^{l+} \\ \vec{E}_m^{l-} \end{bmatrix} = \frac{1}{t_m} \begin{bmatrix} 1 & r_m \\ r_m & 1 \end{bmatrix} \begin{bmatrix} \vec{E}_m^{r+} \\ \vec{E}_m^{r-} \end{bmatrix} \quad (0.9)$$

where, r_m and t_m are the Fresnel reflectance and transmittance in the m-th interface, which is dependent on polarization and angle of incidence. When the field reaches the end of a layer, a phase shift is introduced in the electric field. This can be expressed as,

$$\begin{aligned} \begin{bmatrix} \vec{E}_m^{r+} \\ \vec{E}_m^{r-} \end{bmatrix} &= \begin{bmatrix} e^{i\delta_{m+1}} & 0 \\ 0 & e^{-i\delta_{m+1}} \end{bmatrix} \begin{bmatrix} \vec{E}_{m+1}^{l+} \\ \vec{E}_{m+1}^{l-} \end{bmatrix} \\ &= \frac{1}{t_{m+1}} \begin{bmatrix} e^{i\delta_{m+1}} & 0 \\ 0 & e^{-i\delta_{m+1}} \end{bmatrix} \begin{bmatrix} 1 & r_{m+1} \\ r_{m+1} & 1 \end{bmatrix} \begin{bmatrix} \vec{E}_{m+1}^{r+} \\ \vec{E}_{m+1}^{r-} \end{bmatrix} \\ &= \mathbf{T}_{m+1} \begin{bmatrix} \vec{E}_{m+1}^{r+} \\ \vec{E}_{m+1}^{r-} \end{bmatrix} \end{aligned} \quad (0.10)$$

where $\delta_m = |\vec{k}_0| n_m d_m$ is the phase thickness, $|\vec{k}_0|$ is the wavenumber in vacuum, n_m and d_m is respectively the refractive index and thickness of the m-th layer. The 2×2 matrix \mathbf{T}_m combine all the effect of m-th layer. If this equation is recursively applied, we find the relation between the incident and transmitted field.

$$\begin{aligned} \begin{bmatrix} \vec{E}_0^{r+} \\ \vec{E}_0^{r-} \end{bmatrix} &= \mathbf{T}_1 \mathbf{T}_2 \dots \mathbf{T}_N \begin{bmatrix} \vec{E}_N^{r+} \\ \vec{E}_N^{r-} \end{bmatrix} \\ &= \prod_{i=1}^N \mathbf{T}_i \begin{bmatrix} \vec{E}_N^{r+} \\ \vec{E}_N^{r-} \end{bmatrix} \end{aligned} \quad (0.11)$$

The product $\mathbf{T} = \prod_{i=1}^N \mathbf{T}_i$ of all the individual transfer matrices is called the system transfer matrix.

As the last N th layer will not have any backward directed wave, we have $\vec{E}_N^{r-} = 0$. If we take $\mathbf{T} =$

$\begin{bmatrix} T_{00} & T_{01} \\ T_{10} & T_{11} \end{bmatrix}$, then we have from equation 0.11,

$$\vec{E}_0^{r+} = T_{00} \vec{E}_N^{r+}, \vec{E}_0^{r-} = T_{10} \vec{E}_N^{r+} \quad (0.12)$$

So, the complex reflection and transmission coefficients of the multilayer medium becomes,

$$r = \frac{\vec{E}_0^{r-}}{\vec{E}_0^{r+}} = \frac{T_{10}}{T_{00}} \quad (0.13)$$

$$t = \frac{\vec{E}_N^{r+}}{\vec{E}_0^{r+}} = \frac{1}{T_{00}} \quad (0.14)$$

The reflectance and transmittance of the system are given by $R = |r|^2$ and $T = |t|^2$, which are dependent on polarization, wavelength and angle of incidence for a given structure.

The reflectance seen from the back side of the structure for different widths of sample layer calculated by the transfer matrix method are presented in Figure 2.4. Notice the increase of number of minima with increase in sample layer thickness. Also, minima in p and s polarization reflectance curves are interlaced. The transmittance seen from the front side has their maxima at the angles where back side reflectance curves has their minima.

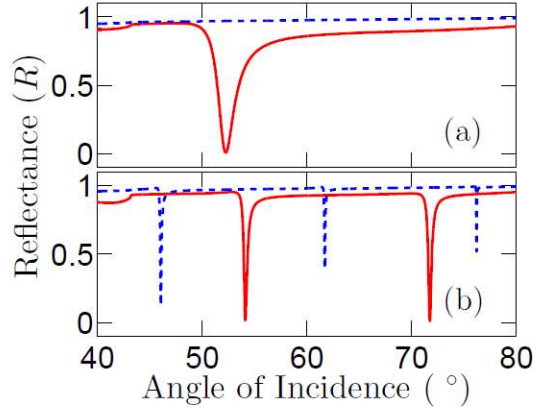


Figure 2.4: Reflectance of the multilayer structure for different angle of incidence are shown. Sample layer thickness in (a) and (b) is 37 and 745 nm. The unbroken and dashed lines are for p and s-polarization respectively. The angles where minima of reflectance occur come with alternating polarization.

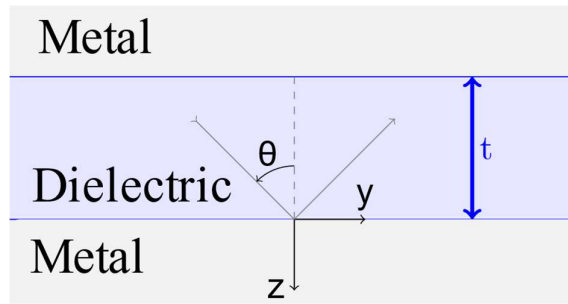


Figure 2.5: Confined Fabry-Perot Resonator - A dielectric layer of thickness t and refractive index ϵ_d inserted between two ideal metal layers.

2.4.3 Fields in the Prism Side

To determine the electromagnetic fields in the prism side, the superposition principle has to be applied. All the decomposed plane waves that add up to the field of the radiating dipole reflect and transmit through the multilayer structure and are emitted in the back and front side. They are weighted accordingly with the reflectance and transmittance calculated by the transfer matrix method. Only the plane waves who have their incident angle and polarization in the minima of the Reflectance curve are transmitted to the back side. This explains the sharply directed angular emission we see, known as Surface Plasmon Coupled Emission (SPCE). The whole structure

works as a multi-notch filter, allowing certain \vec{k} with specific angle and polarization to pass thorough and rejecting all others. As reflectance curve minimums are found at different interlaced angles for different polarizations, the emissions that comes out in the back are highly polarized. This explains the interlacing property of polarization found in the rings in observation plane.

2.4.4 Modes Present in the Structure

Suppose, we have a dielectric layer of finite thickness in \hat{z} direction, but infinite in \hat{x} and \hat{y} direction, which is covered by layers of perfect electric conductor (PEC) as shown in Figure 2.5. This creates a confined Fabry-Perot Resonator (FPR). We calculate the allowed modes in this system by ray optics method. Consider a plane wave with incident angle θ with the normal \hat{z} direction. If the wavelength of the incident light is λ in vacuum, it becomes $\lambda/\sqrt{\epsilon_d}$ in the considered nonmagnetic dielectric. As the electric field is zero inside PEC, all the allowed modes must have standing wave pattern in the \hat{z} direction. Such standing wave pattern is supported if the values of θ satisfies the following equation [24].

$$t = \frac{n\lambda}{2\sqrt{\epsilon_d} \cos(\theta)} \quad (0.15)$$

where, ϵ_d and t are the relative permittivity and thickness of the dielectric layer, λ is the wavelength in vacuum, and $n \in N$ is an integer.

The structure we use for SPCE, has a spacer layer (thickness t_s) which has air in one side and nonideal metal (Silver) in other side. This makes it a partially closed Fabry-Perot interferometer. If we consider an ideal FPR with thickness t_s and refractive index ϵ_s same as the sample layer as the dielectric layer, then the the supported angle θ_{FPR} can be calculated by,

$$\theta_{FPR} = \cos^{-1} \left[\frac{n\lambda}{2\sqrt{\epsilon_s} t_s} \right] \quad (0.16)$$

We show θ_{FPR} along with the s and p polarized SPCE angles for various sample layer thickness in Figure 2.6.

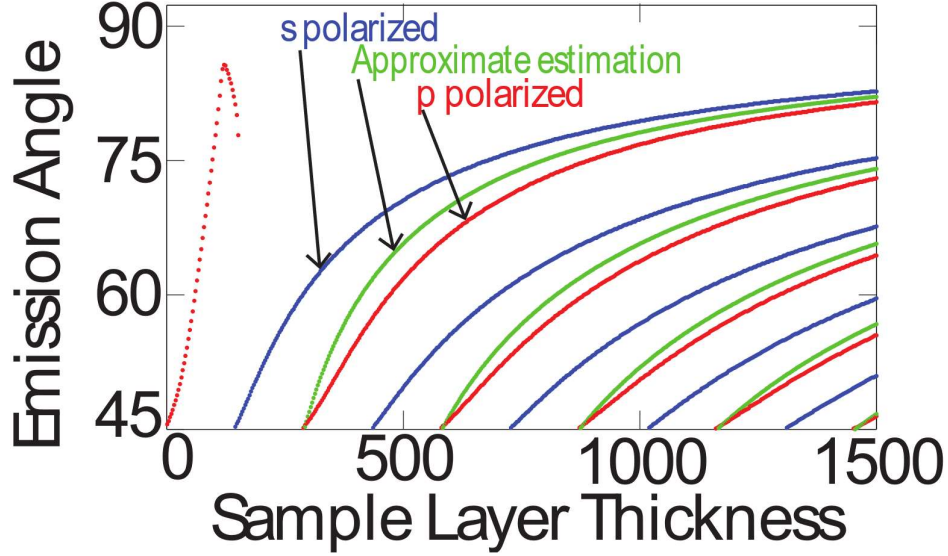


Figure 2.6: θ_{FPR} with s and p-polarized emission angles for different sample layer thickness. Note at 150 nm the emission angle changes discontinuously and polarization changes abruptly.

The striking similarity of the FPR curve with the SPCE angle curves indicates that, those emission angles are mainly result of Fabry-Perot modes existing in the sample layer. But for low thickness, there is a p-polarized SPCE angle curve which has no FPR counterpart to it. The angles in this curve are result of direct emission from SPR, Fabry-Perot modes has no effect in this emission. The previous discussion suggests that, there is a critical thickness t_{crit} above which the SPCE becomes Fabry-Perot mode dominant and below which SPCE becomes SPR mode dominant. Our FDTD simulation and theory predicts that critical thickness to be around 150 nm for our choice of materials and thickness of the metal layer. Experiment also reported that if sample layer thickness is increased than 160 nm, the emission suddenly becomes s-polarized from p-polarized and the emission angle drastically changes [8]. We claim that, this is due to the fact that, after the critical thickness the Fabry-Perot mode becomes dominant and SPR has no longer any significant effect in the emission. To prove it, we replaced the metal layer with a dielectric layer with high refractive index. If SPR were necessary for the emission, then p-polarized angular directional radiation would not come out in the back side for any thickness. But beyond the critical thickness, p-polarized emission occurs even for dielectric materials. This clearly proves that, SPR is not necessary for SPCE after sample layer thickness reaches above critical thickness, as dielectric layers cannot sustain SPR. The authors would like to point out that, this is contrary to the current explanation of SPCE [13]. It was thought that, hybrid SPR-Fabry-Perot modes are responsible for p-polarized emission. But from our simulation, it is clear that, under critical thickness SPR is responsible for p-polarized emission and above critical thickness Fabry-Perot modes are responsible. That's why if metal layer is replaced by a dielectric layer, p-polarized emission below t_{crit} is not found as

there are no SPR. It is only found for sample thickness above t_{crit} for which there is no SPR but Fabry-Perot modes. This does not mean, when sample layer thickness is greater than t_{crit} and metal layer is used, SPR does not occur there. SPR is present whenever there is metal, it just has no effect on the emission. The s-polarized emission is the direct result of Fabry-Perot modes. These emission is available when sample thickness is above critical thickness. Below t_{crit} there is no s-polarized emission as SPR cannot be excited for s-polarized light. The presence of s-polarized emission angles after t_{crit} and their similarity with the p-polarized emission angles is also a proof of that, similar mechanism is responsible for their emission, namely the Fabry-Perot modes.

2.4.5 Approximate Estimation of Emission Angle

We have come up with approximate empirical formulas for s and p polarized emission angles (θ_s and θ_p) if the sample layer thickness is greater than t_{crit} . If the thickness of the metal layer t_m , then the empirical formulas are,

$$\theta_p = \cos^{-1} \left[\frac{n\lambda}{2\sqrt{\epsilon_s} (t_s - t_m)} \right] \quad (0.17)$$

$$\theta_s = \cos^{-1} \left[\frac{n\lambda}{2\sqrt{\epsilon_s} (t_s + t_m)} \right] \quad (0.18)$$

where n is an integer. For larger thickness the approximate formula gives the emission angle with an error ≤ 5 degrees and can exactly estimate the number of s and p polarized emission angles. These works very handy for fast calculations without the need of any complex and time-consuming simulations.

2.5 Summary

This chapter explains the background theoretical ideas needed to understand SPCE. Transfer matrix method (TMM) delivers the transmitted electric field when a plane wave is incident on a multilayer structure. Expanding the radiation from the fluorescent molecule in a superposition of plane waves with different wavevector, polarization and amplitude. By weighing the plane waves with appropriate complex reflection and transmission coefficients found by TMM and then superimposing them, we can find the radiation emerging in the prism side. The simulation can

easily be implemented in MATLAB. Further analysis shows, the plane waves that are dominant in the prism side are the ones who have their wavevectors in the reflectance minimum direction. SPCE occurs at the angles where reflectance is minimum. For thin sample layers, SPCE occurs only in one angle and the radiation is p-polarized. The mode is SPR dominant. After the thickness exceeds a critical value, coupled SPR Fabry Perot modes occur. This leads to SPCE in multiple angles in alternating polarization. The developed theory is an established method of solving fields for dipoles in any stratified media and for our problem, it gives satisfactory result.

Chapter 3

Simulation Method

In this work, finite difference time domain (FDTD) has been used to design and analysis the performance of difference SPCE structures. FDTD is an implementation of Maxwell's time-dependent curl equations for solving the temporal variation of electromagnetic waves within a finite space that contains a target of arbitrary shape and has recently become the state-of-the-art method for solving Maxwell's equations for complex geometries. Since FDTD is a direct time and space solution, it offers the user a unique insight into all types of problems in electromagnetics and photonics. Furthermore, FDTD can also be used to obtain the frequency solution by exploiting Fourier transforms; thus, a full range of useful quantities in addition to fields around particles can be calculated, such as the complex Poynting vector and the transmission/reflection of light.

In the FDTD technique, Maxwell's curl equations are discretized by using finite difference approximations in both time and space that are easy to program and are accurate. To achieve high accuracy for realizing the spatial derivatives involved, the algorithm positions the components of the electric and magnetic field about a unit cell of the lattice that constitutes the FDTD computational domain. Each individual cube in the grid is called the Yee cell.

The previous chapter described a structured method to estimate the number of SPCE angles and their values. This chapter sheds light to the SPCE mechanism by analyzing the structure in detail using FDTD method. As FDTD is capable of providing the value of fields in any instant and in any position inside the structure, we were able to study the mechanism of SPCE with much greater detail. Modelling of the system are presented before the description of results from FDTD and other simulations.

3.1 Simulation Model

The basic structure used in SPCE generation has already been discussed in theory section. A schematic diagram is shown in Figure 2.1. 50 nm Silver is deposited on a hemispherical glass (SiO_2) prism. The sample layer contains the fluorescent molecules. The spacer layer sits between

the metal and sample layer. Air is the bulk material. In this section, we discuss the modelling of this basic structure in FDTD simulator, providing parameters used in the simulation and mesh independence test.

3.1.1 Material modelling

Modelling of materials in FDTD is done via experimental values of complex refractive index measured at sampled wavelength values. For intermediate arbitrary wavelength, interpolated values are used. Silver (Ag) was used as the metal layer in our simulation. Modelling of metals is very critical in FDTD as their parameters vary substantially in different datasets. We used data obtained by Palik [25] to model Ag. The experiments used PVA (Poly Vinyl Alcohol) as the medium which contained the molecules. Due to unavailability of experimental values of frequency behavior of PVA dielectric constants we used glass instead as sample layer. The reason behind this is that the better studied glass closely resembles PVA when their optical properties are compared. This was also exercised in previous theoretical works [12], [13]. We used Palik's [25] data for glass as it is very reliable. Later when specific fluorophores and effect of their environment were considered, other materials like water [26], ethanol [27] were also used as sample layer. Substrate air was modelled by constant refractive index of 1.

3.1.2 Fluorophore modelling

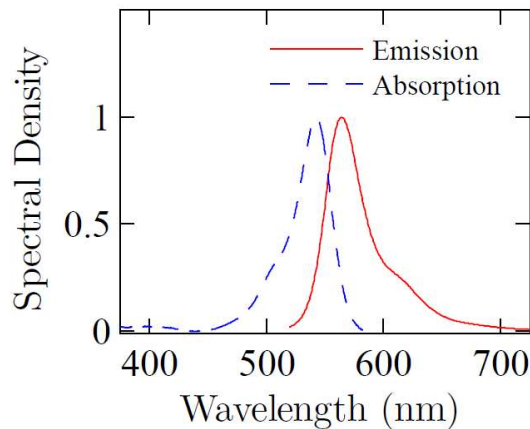


Figure 3.1: Experimental emission and absorption spectrum of Rhodamine B[28]. The difference between maximum emission and extinction wavelength, called stokes shift, is around 22 nm.

Fluorophores are chemical compounds that emit light while they are excited. They absorb electromagnetic energy of a specific wavelength and re-emit light at a longer wavelength. Each of them has their own distinct absorption and emission spectral profile, which depends both on the structure of the molecules and their chemical environment. The spectrum of Rhodamine B is shown on Figure 3.1. An excited fluorophore can be considered mathematically equivalent to an electric dipole, as it emits light in a wavelength range much larger than the physical dimension of the emitter itself [19]. The lifetime of the fluorophore is the time it spends on average in the excited state before returning to the ground state. The frequency characteristic and lifetime of a specific dye can be modelled by an electric dipole, whose emission has the same frequency components and luminescence duration is equal to the lifetime. FDTD simulation returns multiple frequency data at a single simulation run. Simulation of an arbitrary broadband dipole in the structure, can deliver time domain fields of monochrome, unity amplitude dipoles $\vec{E}(\vec{r}, t, \lambda)$ for a range of wavelengths λ . If the emission spectrum (energy radiated various wavelength) of a specific fluorophore is $P(\lambda)$, then the electric field of this molecule when placed in the structure can be calculated by $\int_0^\infty d\lambda \sqrt{P(\lambda)} \vec{E}(\vec{r}, t, \lambda)$. Once the fields are evaluated, emission angles and other parameters for various fluorophores like Rhodamine, Cyanine can be acquired.

3.1.3 Simulation Dimension

Memory and time requirements in FDTD simulation increases very rapidly with the increase of simulation volume. Although larger simulation region would lead to better accuracy, it is not always possible given finite computational resource and time. Our simulated structure has 20 μm span in x and y direction and 16 μm span in z direction. The metal layer, which is 50 nm thick, is situated from $z = -70$ to $z = -20$ nm. The dipole is positioned at the origin. For FDTD to work, it is necessary to discretize the structure, the finer the meshing the better. But fine meshing will again increase the memory requirements, so non uniform meshing is required for optimum performance. As plasmon and SPCE generation occurs in metal glass interface, it is meshed finely. Grid points near the interface are separated by maximum 4 nm. Points in substrate and prism are maximum 50 nm apart in all direction. Sample layer-substrate interface is also meshed with smaller grid (maximum 10 nm).

3.1.4 Mesh Independence Test

The validation test of the FDTD simulations are done by matching the experimentally found and theoretically predicted values with the simulation results. The matched results validated the simulation procedure. To maintain the accuracy and stability of the FDTD calculations, mesh independence test was done by first finding the threshold mesh size. The threshold mesh size the largest grid size to accurately model the prescribed system without being computationally prohibitive. Traditionally, it is obtained in an iterative fashion (convergence testing). By starting from a very small mesh size, it was increased until the simulation gave diverging results. The lowest mesh size which gives diverging results are the threshold mesh size. We chose a spatial mesh size so that, it is smaller than the threshold mesh size and the halving of this mesh size, although increases the simulation time considerably, yields same results. FDTD algorithm requires the time increment have a specific bound relative to the spatial discretization ($\Delta t/\Delta x$) to ensure the stability of the time-stepping algorithm. In our implementation of FDTD, the time step of the simulation is determined by the values of the spatial grid to ensure numerical stability and the user has the flexibility to set the total time of the simulation. Additional time-domain monitors provided time-domain information for the various field components within the FDTD simulation region over the entire course of the simulation. At the end of the simulation, the various field components are checked to see if they decay to zero, thus indicating that the simulation has run for a sufficiently long time for the CW information to be valid.

3.1.5 Boundary Conditions

The whole structure is much larger than the wavelength in consideration and taken to be infinite in extent in all direction for simulation purposes. This requires the use of perfectly matched layer (PML) boundary condition outside the structure [29]. PML absorbs the wave that is incident on it, thus simulating an infinite region. It requires the whole structure to be simulated, which is both time and memory consuming. But with proper use of symmetric and anti-symmetric boundary conditions in lateral directions, correct results can be found with one-fourth time and memory. Symmetric (or anti-symmetric) boundary condition, when used in any direction, divides the simulation region in 1/2 and assigns the noninverted (or reversed) values of fields calculated in one half to the other.

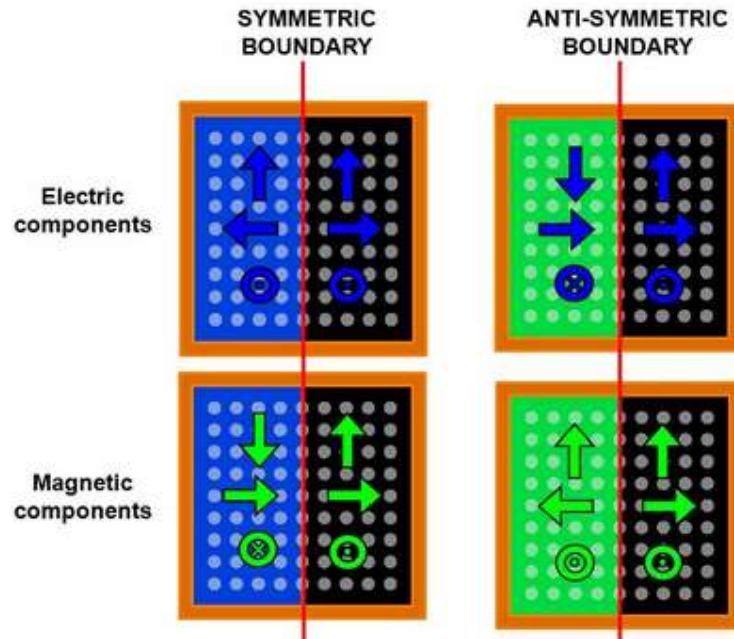


Figure 3.2: Fields at symmetric and antisymmetric boundary conditions.

For vertical dipole with its moment in \hat{z} direction, symmetric boundary conditions are used in \hat{x} min and \hat{y} min direction, as electric field is tangent on both xz and yz plane ($\phi = 0^\circ$ and $\phi = 90^\circ$). For horizontal dipole with moment in \hat{x} direction, electric field is normal to yz plane but lies on xz plane ($\phi = 0^\circ$). So symmetric and anti-symmetric boundary condition is used in \hat{y} min and \hat{x} min directions respectively. PML is still used in \hat{z} , \hat{x} max and \hat{y} max direction. Used PML layer must have substantial number of layers as electric field will be incident on it with steep angle. Used boundary conditions are shown in Figure 3.2 for both horizontal and vertical moments.

3.1.6 Farfield Calculation

As it is not possible to simulate large enough region to observe farfield, it is calculated by projecting near field into a hemisphere of large radius. This is done by the Huygens principle. The principle states that, if the value of a field, which obeys Helmholtz equation and its gradient in the normal direction of the surface which contains the origin volume is known, the field is known in the infinity.

To calculate a far-field projection of an electromagnetic field in a plane, it is first Fourier transformed and broken into constituent plane waves. These plane waves have differently directed

wave vectors and amplitudes. These plane waves are extended and propagated a large distance (1 meter in our case) through the media. Propagation of plane waves does not need large simulation, as it just adds only a phase. Then they are again superimposed to form the far field projection. In our case, field crossing a plane placed in $z = 300$ nm is projected in a distant plane.

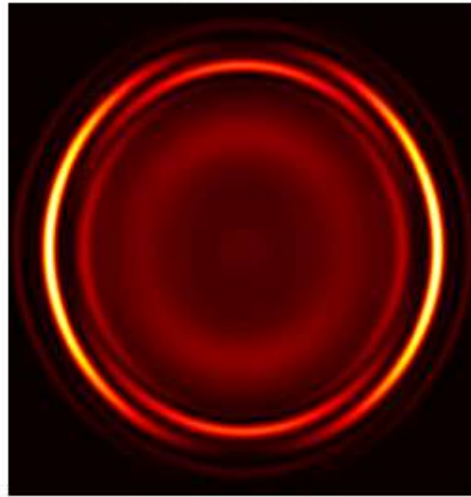
3.2 Simulation Results

The far-field projection shows the characteristic rings of SPCE as observed in experiments. Number of emission angles and their values found from many experiments, predicted theoretical values and our FDTD simulation matches.

The radiation pattern in the observation plane in Figure 2.2 of a single dipole with moment \hat{p} in \hat{z} and \hat{x} direction is shown in Figure 3.3a and Figure 3.3b. If the dipole moment is in the \hat{z} direction in Figure 2.1, then it emits p-polarized light in any azimuthal direction. So SPCE is only found in only the p-polarization reflectance minimum angles. If the dipole moment is in the interface plane, without any loss of generality we can assume the dipole moment is in \hat{x} direction, as the structure is azimuthally homogeneous. Now the dipole emits p-polarized light close to \hat{x} direction but s-polarized light in \hat{y} direction. So, if the far field is observed in azimuthal angle $\phi = 90^\circ$, SPCE is found only in the s-polarization reflectance minimum angles. But in $\phi = 0^\circ$, only p-polarized SPCE is observed. Vertical dipoles only emit in p-polarized SPCE, but horizontal dipoles emit both p and s-polarized SPCE. Figure 3.3a and Figure 3.3b, which are the hemispherical observation plane seen for \hat{z} and \hat{x} directed dipoles in a sample layer thickness 745 nm, clearly displays the above explained properties. From Figure 2.4, at 745 nm we expect three p-polarized and three s-polarized emission. Both the horizontal and the vertical dipole shows three p-polarized emission angles, the lowest of which is barely visible. The reason of such weak emission is a non steep reflectance minimum at that angle. The three s-polarized emissions are found only in the vertical dipoles far field, for the reasons explained above.



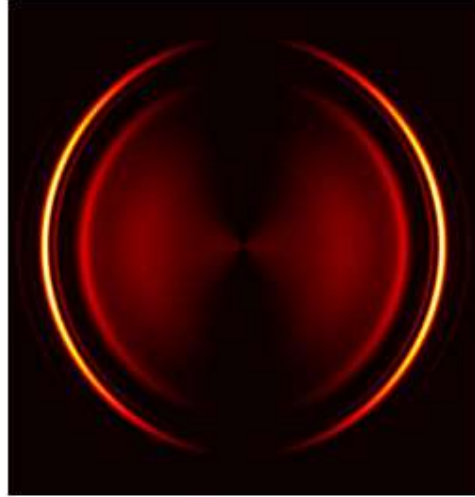
(a) Vertical Dipole



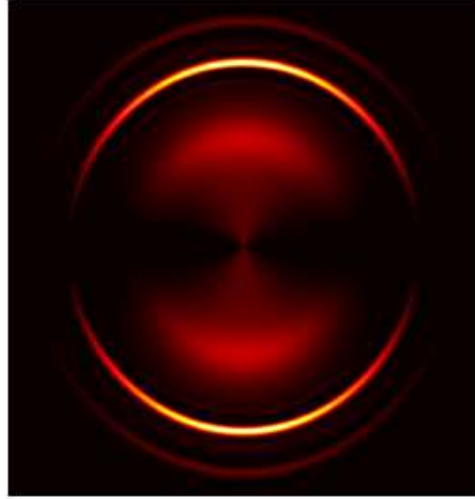
(b) Horizontal Dipole

Figure 3.3: Far field radiation intensity of a vertical and horizontal dipole inside the prism projected in a hemispherical observation plane. The vertical dipole only shows p-polarized emissions where the horizontal dipole shows both p and s-polarized emission.

Power per steradian of a horizontal dipole for various θ observed in $\phi = 0^\circ$ and $\phi = 90^\circ$ planes are shown in Figure 3.5. Figure 3.5a, which is actually the cross section of Figure 3.3b in \hat{x} direction, shows all the p-polarized emission angles and Figure 3.5b, which is actually the cross section of Figure 3.3a in \hat{y} direction, shows all three s-polarized emission angles.



(a) $|E_\theta|^2$



(b) $|E_\phi|^2$

Figure 3.4: $|E_\theta|^2$ and $|E_\phi|^2$ horizontal dipole measured in far field. The intensity is shown in Figure 3.3b. $|E_\theta|^2$ is maximum in the direction of p-polarized emission. $|E_\phi|^2$ is maximum in the direction of s-polarized emission.

Normalized radiation intensity with respect to θ is displayed in Figure 3.6. P and s-polarized peaks are found in x-z and y-z planes, respectively. The polarization interweaving of peaks are visible. Electric field in the rings are found to be highly polarized as observed in the experiment. Figure 3.4 shows $|E_\theta|^2$ and $|E_\phi|^2$ for a horizontal dipole with $\hat{p} = \hat{x}$. As s-polarized emission occurs in

\hat{y} or $\phi = 90^\circ$ direction, $|E_\phi|^2$ shows its maximum in that way at the angles of s-polarized emission. $|E_\theta|^2$ reaches its maximum at p-polarized reflectance minimum angles in the \hat{x} direction.

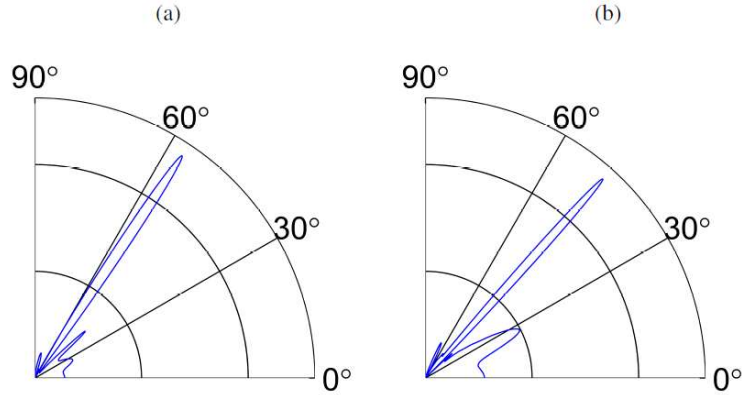


Figure 3.5: Power per solid angle of a horizontal dipole seen in a plane containing the dipole moment ($\phi = 0^\circ$) and normal to the dipole moment ($\phi = 90^\circ$).

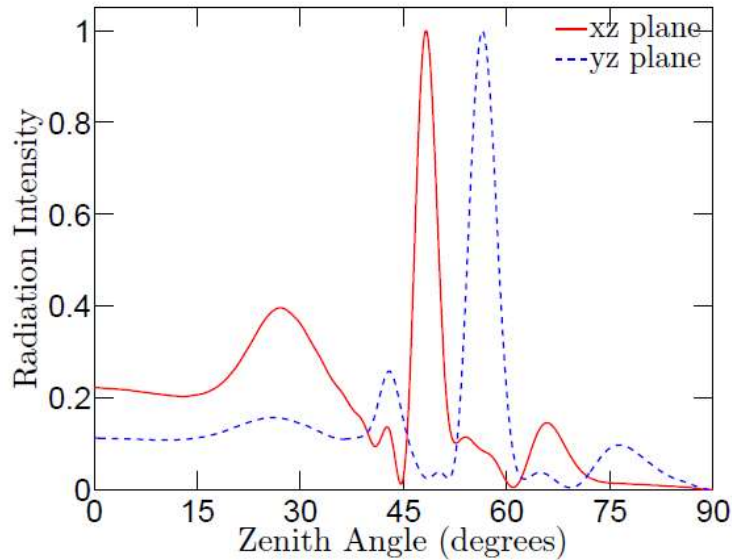


Figure 3.6: Electric field intensity (normalized) in various zenith angle of a horizontal dipole seen in xz plane containing the dipole moment ($\phi = 0^\circ$) and in yz plane normal to the dipole moment ($\phi = 90^\circ$). The s and p-polarized peaks occurs at interlaced angles.

If multiple dipoles are present in the structure, which is always the case in experiments, they have random orientations. All of them can be expressed as a summation of some vertically and horizontally oriented dipoles. Vertical dipoles contribute to the p-polarized rings. Single horizontal

dipole has semicircular emission outline. Randomized horizontal dipoles has their dipole moment in all the lateral directions (along all ϕ for $\theta = 90^\circ$), so their semicircles connect up and construct the s-polarized continuous ring detected in experiment.

3.3 Summary

FDTD simulation is a general computational electromagnetics tool that can simulate very general structures. Interest in FDTD Maxwell's equations solvers has increased nearly exponentially over the past 20 years. Increasingly, engineers and scientists in non-traditional electromagnetics-related areas such as photonics and nanotechnology have become aware of the power of FDTD techniques. Yet to the best of our knowledge, we simulated SPCE by complete 3D FDTD method for the first time. FDTD has lead us to results that are theoretically and experimentally expected. Simulation of much complicated photonics structures for SPCE enhancement will be possible with FDTD method.

Chapter 4

Single Molecule Detection with Nanostructures

Detection of single molecules represents the ultimate level of sensitivity and has been a longstanding goal of analytical methods. Because of its high sensitivity, and because of bright signal appears against a dark background, fluorescence is one obvious choice for single molecule detection (SMD). However, SMD using fluorescence is technically difficult, particularly in less pure biological samples [30]. In any real system, there will be background signal due to impurities in the sample, emission from optical components, scattered light at the incident wavelength, and dark current from the detector. Additionally, the intrinsic Raman scattering makes it challenging for SMD. Therefore, SMD has to be performed in a restricted volume.

Surface plasmon coupled emission (SPCE) based fluorescence microscopy technique can be used for SMD for its capacity to restrict the sample volume that is excited [6]. In this approach, target molecules are fluorescently labelled and are placed on a thin metal layer, which is deposited on a glass prism [17]. The fluorescent molecules are excited by an incident light on the metal surface from the prism side, which couples to surface plasmon resonance (SPR) in the sample side. Once excited by the light coupled to SPR, fluorescent molecules radiate like dipoles. A part of the radiated light may couple to the metal layer and create coupled SPR in the other side of the metal. The excited SPR modes by the fluorescent molecules are leaky and radiates a light cone with sharply defined half angle. This phenomenon is called SPCE [2], [11], [12], [21], [31].

Since fluorescent molecules are excited by an exponentially decaying SPR coupled light, the detection volume and hence the background noise can be limited in SPCE. Additionally, power coupled to SPCE decreases exponentially with distance of the fluorescent molecule from the metal layer when the distance is greater than a critical value [22]. Therefore, SPCE is a promising candidate for SMD. However, although SPCE emits light only in a sharply defined angle, the intensity of the emitted light is less due to loss in metal [5]. Therefore, detectivity is difficult when the excitation volume is very limited as in for SMD.

The pursuit of increasing the coupled power to SPCE is an active area of research [32]. Two techniques can be used to increase the coupled power: First, by changing the sample layer or the surface of the structure so that the fluorescence of the fluorescent molecules is enhanced. Second, by engineering the metal-dielectric structure so that the coupling of fluorescence to SPCE can be increased. Till date, there have been many efforts to increase the fluorescence. Colloidal metal nano particles suspended in the sample layer are formed to increase the SPCE ~35 times by increasing fluorescence [33]. Recently, carbon nano dots (AgCD) are found to increase fluorescence as much as 1000 times, setting the benchmark for fluorescence techniques [16]. Power coupled to SPCE has also been increased by using a grating on the metal layer and using metal bi-layers of silver and gold [15], [34]. The collection efficiency of SPCE can also be increased by using external means such as a conical mirror around the hemispherical prism so that SPCE ring is reflected into a single point [15].

In this work, we propose a nanostructure that significantly increases the power coupled to SPCE and decreases the excitation volume of the sample so that it helps SMD. In the proposed structure, instead of a metal layer, we use a metal layer with nanoholes.

4.1 Proposed Structure

In Figure 4.1, we show schematic illustrations of a typical structure that supports. In the typical structure, a 50 nm silver (Ag) layer is deposited on a hemispherical Silicon Dioxide (SiO_2) glass prism. A 10 nm SiO_2 layer is deposited on the metal layer that acts as a spacer between the metal and fluorescent molecules. The sample layer containing the fluorescent molecules are placed on the spacer layer.

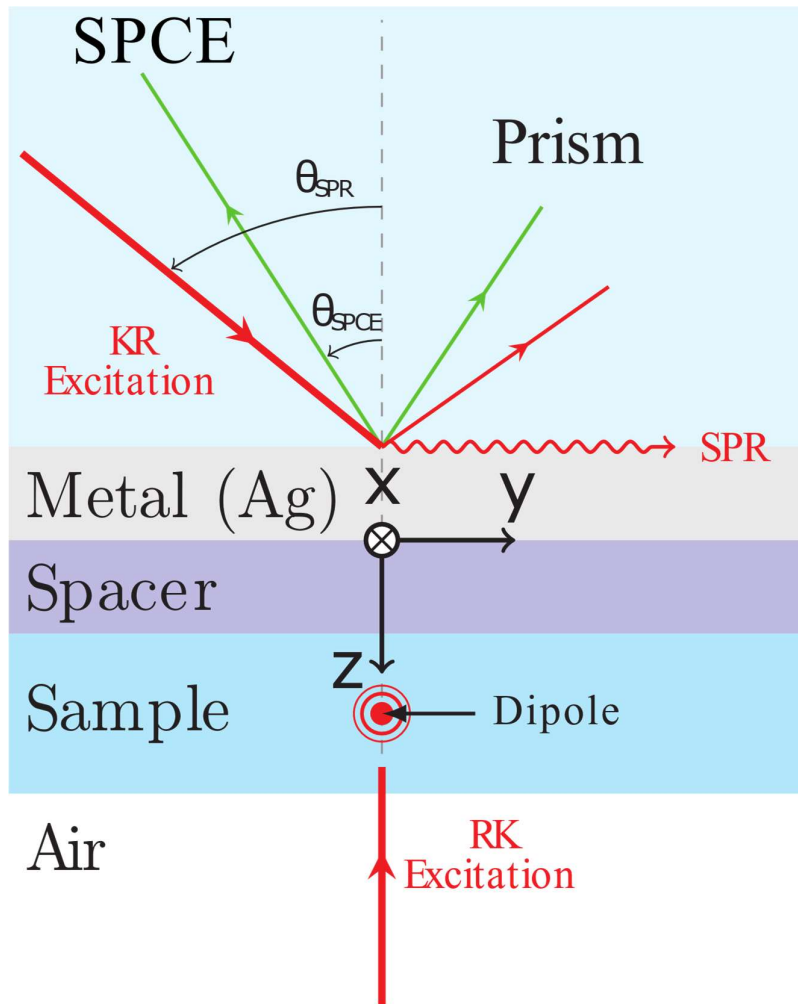


Figure 4.1: Structure used for SPCE generation with different excitation schemes

In the proposed structure, instead of a simple silver layer, we use a silver layer with nanoholes, which is shown in Figure 4.2.

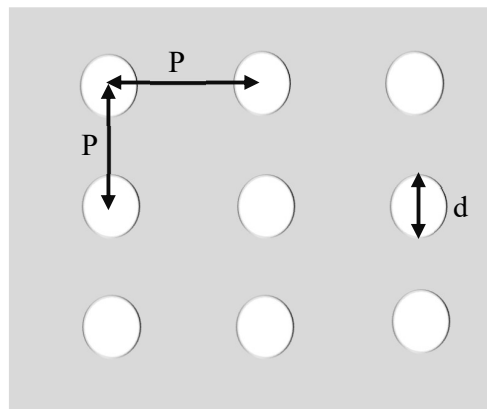


Figure 4.2: Metal with nanoholes. The period of the nanohole array is P and the diameter of a nanohole is d .

In the proposed structure, we keep the metal layer thickness 50 nm – same as that of the typical structure. The length of the nanoholes is equal to the metal layer thickness. The periodicity of the nanoholes is P and the diameter is d . We vary P and d to garner the response we desire.

In this work, we use a Polyvinyl alcohol (PVA) layer of 30 nm as the sample layer. We also use Rhodamine B as the fluorescent molecule. Rhodamine B molecules have a peak absorption at a wavelength of 545 nm and a peak emission at 565 nm. Therefore, we assume to excite the fluorescent molecules with a laser source of 545 nm from the prism side. The excitation laser emits a sharp Gaussian pulse. The fluorescent molecules subsequently emits light at 565 nm in the sample layer, which is coupled to the silver layer. The Rhodamine B fluorescent molecules are modelled as monochrome electric dipoles oscillating at 565 nm. Since the dynamics vary with the position of the fluorescent molecule in the sample layer, we keep the positions fixed so that the performance of the proposed structure can be properly analyzed. In this approach, fluorescent molecules are excited by a laser source from the prism side, which is often referred to as Kretschmann configuration. The fluorescent molecules can also be excited from sample layer side, which is often referred to as Reverse Kretschmann configuration. In Kretschmann configuration, if the p-polarized incident light on the metal layer from the excitation laser matches with a critical angle, θ_{SPR} , surface plasmons are excited and light is evanescently coupled to the metal-sample layer interface. This evanescent light can excite the fluorescent molecules. Since the light coupled to the surface plasmons decays exponentially from the interface, it excites fluorescent molecules that are very close to the interface. Therefore, Kretschmann configuration can be used for detecting monolayer of the sample or single molecule [6].

Once the fluorescent molecules are excited, they emit light as dipoles. This light may couple into metal layer and come out as SPCE in the prism side at an angle θ_{SPCE} . The intensity of SPCE light depends on the intensity of light that excites the fluorescent molecules and the distance of the fluorescent molecules from the metal layer. The luminescence of the fluorescent molecules directly depends on the intensity of the excitation light. The luminescence of the fluorescent molecules also depends on the host medium in the sample layer. The distance dependent coupling of luminescence into SPCE has bell-shaped characteristic with a slowly decaying tail as the distance of the fluorescent molecules from the metal surface increases [14]. If the fluorescent molecules are

within 10 nm from the metal surface, the fluorescence is quenched and significantly less power is coupled as SPCE.

4.2 Fabrication Feasibility

As far as the fabrication is concerned, this nanohole array can be fabricated using photolithography, deep reactive ion etching, wet etching, and focused ion beam lithography techniques as suggested by Rauf et al. [35]. They characterized gold nanohole array using scanning electron microscopy (SEM), cyclic voltammetry (CV), and chronoamperometry (CA); SEM imaging of the arrays showed that each hole is circular at the mouth. Therefore, following the similar procedure we can fabricate the periodic silver nanoholes.

4.3 Dispersion Relation of the Proposed Structure

The control setup for SPCE generation can be considered as a metal slab between different dielectric media (air, PVA, and glass – $\epsilon_{air} \neq \epsilon_{PVA} \neq \epsilon_{glass}$). Dispersion relation for such a thin metal film in an asymmetric environment is well studied and it supports both symmetric and antisymmetric modes [36]. Only symmetric modes are radiative or leaky, which are bounded SPR type in air side, but EM plane wave type in glass side. This is the mode that is created when a plane wave of appropriate wavevector is incident on the metal layer from the glass side. Only such modes are of interest when fluorescent excitation is considered, as laser beam is incident from the glass side in KR configuration and the created SPR decays exponentially in the air side.

The dispersion relation is modified substantially for a structure with nanostructures. To find the dispersion relation of a general structure, one must solve the Maxwell's equations in every region and find the overall solution that satisfies the boundary conditions. Suppose, such structure has $j = 1, 2, \dots, N$ layers (corresponding relative permittivity, ϵ_j) with inhomogeneity in z direction, and the SPR is propagating in the x direction with in-plane wavevector β . Such a plasmon field will have components E_x , E_z and H_y . The governing equations for this TM mode in layer j is,

$$\frac{\partial^2 H_z}{\partial z^2} + (k_j^2 - \beta^2)H_z = 0 \quad (4.1)$$

$$\vec{E} = \frac{i\sqrt{\epsilon_j}}{\omega c} \vec{\nabla} \times \vec{H} \quad (4.2)$$

In every layer, the fields will be a weighted linear combination of the terms $\pm s_j z \pm i\beta x$, where $s_j^2 = k_j^2 - \beta^2$ and $k_j = \sqrt{\epsilon_j} k_0 = \frac{\sqrt{\epsilon_j} \omega}{c}$.

Let us consider the confining layers $j = 1$ (air, $z > 0$) and $j = N$ (glass, $z < 0$). As they are considered infinite, they will have fields proportional to $e^{-s_1 z}$ and $e^{-s_N z}$, respectively. As the mode for excitation light in SPCE geometry must be leaky in glass side, so s_N must be imaginary. As $s_N^2 = \beta^2 - \epsilon_{glass} k_0^2$, this is only possible when the dispersion relation is in the left side of the glass light line. Also the mode is bounded in air side, so s_1 must be real, so the dispersion curve must be in the right side of the air light line. The penetration depth in the axial direction in air is $\frac{1}{s_1}$. As $s_1^2 = \beta^2 - \epsilon_{air} k_0^2$, so the more the dispersion curve moves away in the right side from the air light line, the tighter the mode becomes in the air.

Although the principle stated above is simple enough, finding the dispersion relation in closed form becomes analytically complex if asymmetry and large number of interfaces are present. The number of branches in the dispersion relation increases with the number of interfaces present in the structure. Also, determination of which mode is generated when plane wave is incident is hard. To avoid these problems, we find out only the dispersion relation corresponding to the leaky or radiative mode. To modify the dispersion relation of the typical structure, we make periodic nanoholes in the metal layer. To determine the dispersion relation of this modified structure, we find the reflectance of the structure from the glass side using FDTD method for TM polarized plane wave of specific frequency for all incidence angle (θ) in the range $\left[0, \frac{\pi}{2}\right]$. The incidence angle, $\theta_{SPR}(\omega)$, for which the minimum reflectance is found is the emission angle of the leaky SPR mode. The in-plane wavevector then can be calculated by,

$$\beta(\omega) = k_{glass} \sin(\theta_{SPR}(\omega)) = \frac{\omega \sqrt{\epsilon_{glass}}}{c} \sin(\theta_{SPR}(\omega)) \quad (4.3)$$

Reflectance of the p-polarized light from the prism side is a function of both frequency (ω) and incident angle (θ). For a specific frequency, first we calculate minimum reflectance angle,

$\theta_{SPR}(\omega)$. Then, we use Equation 4.3 to find the in-plane wavevector for that specific frequency. We repeat this procedure for a range of frequency and generate the dispersion relation.

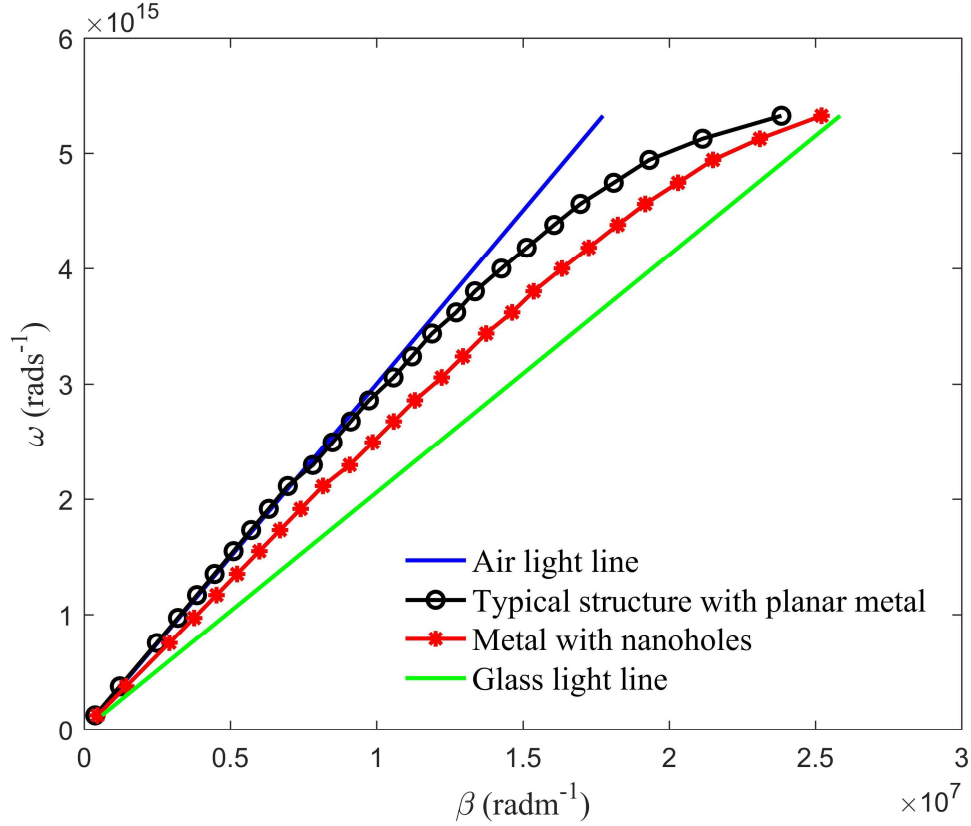


Figure 4.3: Frequency (ω) vs in-plane wavevector (β) or dispersion relation. Only the leaky modes are shown. Left and right most straight lines are light lines of air and glass, respectively. The in-plane wavevectors for typical structure and proposed structure with nanoholes – $P = 520 \text{ nm}$ and $d = 170 \text{ nm}$ – lie between the air and glass light lines.

Figure 4.3 shows the dispersion relation of the proposed structure. We see that the dispersion curve lies right to the typical structure. It implies that the excitation field is tightly bound to the metal-sample layer interface. This results in a smaller penetration depth, hence a smaller detection volume. As we find it promising, we move forward to find the excitation field to calculate the penetration depth.

4.4 Penetration Depth

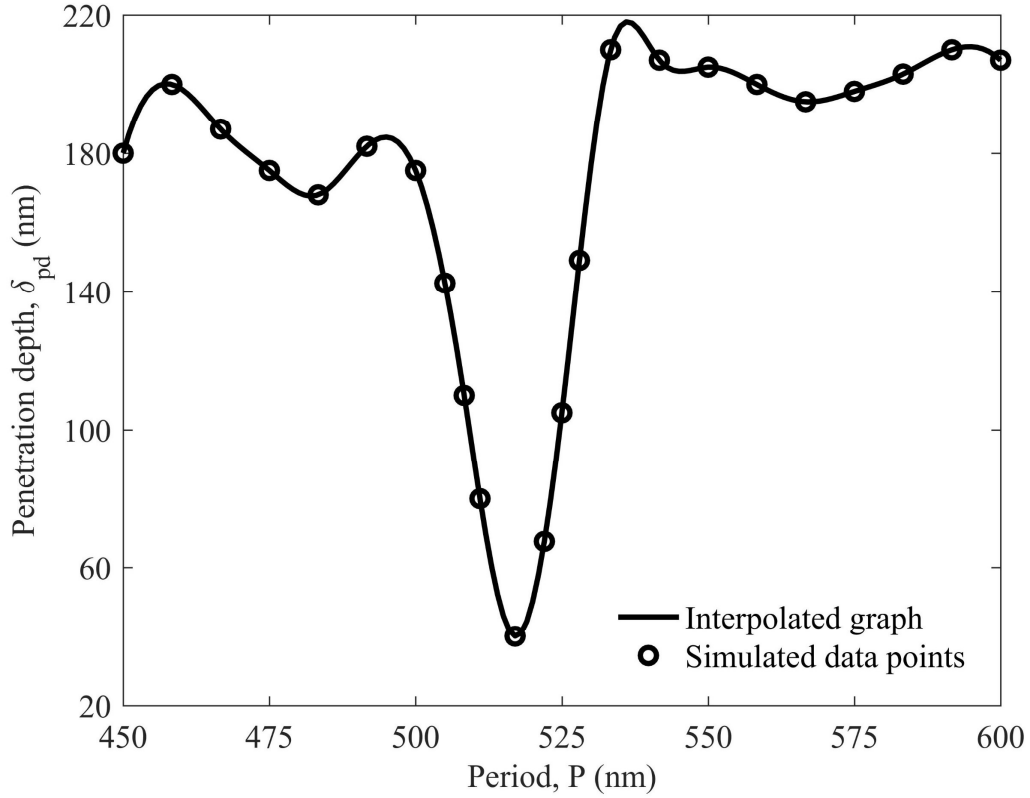


Figure 4.4: Penetration depth δ_{pd} vs Period of the nanoholes. Diameter of the nanoholes is considered to be 170 nm. The penetration depth shows a steep deep, which occurs at $P = 520$ nm. At this point the penetration depth is only 40 nm that is very suitable for single molecule detection, whereas typical structure has a penetration depth of around 250 nm.

The penetration depth of a typical SPCE structure shown in Figure 4.1 is around 250 nm, i.e., the excitation field decays to e^{-1} of its value at the sample-air interface at 250 nm away from the interface. We calculate the penetration depth (δ_{pd}) for the proposed structure – with nanoholes in metal layer – shown in Figure 4.2 as a function of periodicity, while the diameter of the nanoholes is 170 nm, a constant value. The curve shows a minimum at $P = 520$ nm, and the minimum value is significantly lower than the typical values. We use particle swarm algorithm to find the global minimum value of penetration depth. Particle swarm algorithm varies period and diameter of the nanoholes, and calculates respective penetration depth to find the optimum combination of period and diameter of the nanoholes.

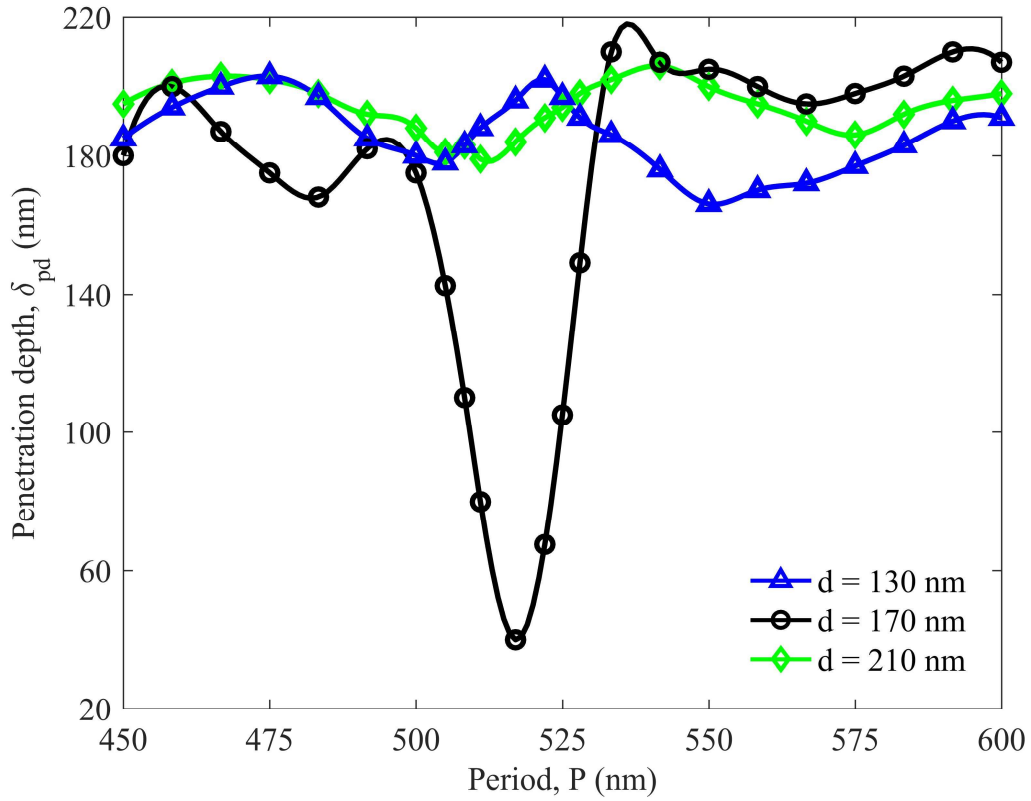


Figure 4.5: Penetration depth (δ_{pd}) vs period (P) of the nanoholes for different three different diameters of the holes. Blue triangle, black circle, and green diamond represent the graph for nanoholes diameter of 130, 170, and 210 nm, respectively. When diameter is 130 nm or 210 nm, there is no significant decrement in penetration depth. However, for a diameter of 170 nm, there is a sharp minimum at around $P = 520$ nm. Lowest penetration depth of 40 nm is achieved at that point.

In Figure 4.5, we note that the penetration depth decreases significantly in the proposed structure. Although there are no significant changes in penetration depth for nanohole diameter size of 130 nm and 210 nm, we find smallest penetration depth for nanoholes diameter size of 170 nm with a periodicity of 520 nm. This result is also found by particle swarm algorithm.

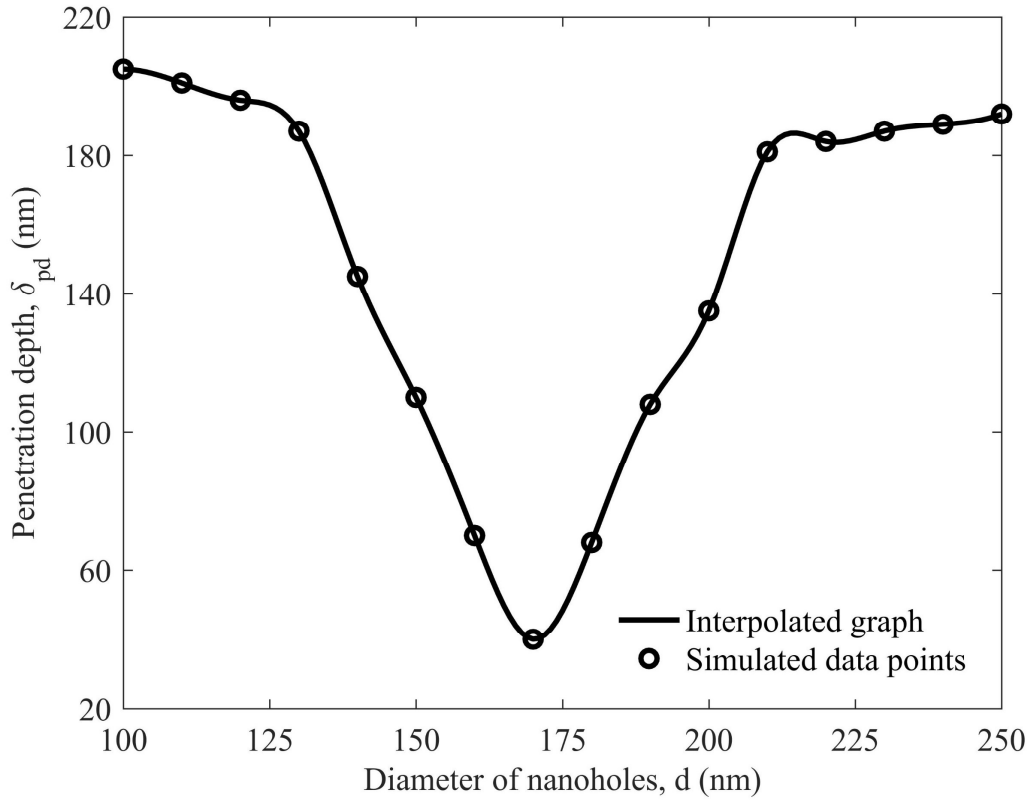


Figure 4.6: Penetration depth (δ_{pd}) vs diameter of the nanoholes, d (nm) for a periodicity of P = 520 nm. This figure shows a minimum at d = 170 nm, confirming our previously found result.

In Figure 4.6, we show the relationship of penetration depth with diameter of the nanoholes for a fixed periodicity of 520 nm. It also exhibits a similar characteristic. There is a deep in the curve at d = 170 nm. The blue dots are simulated data points, whereas the continuous graph is drawn by interpolating the data points.

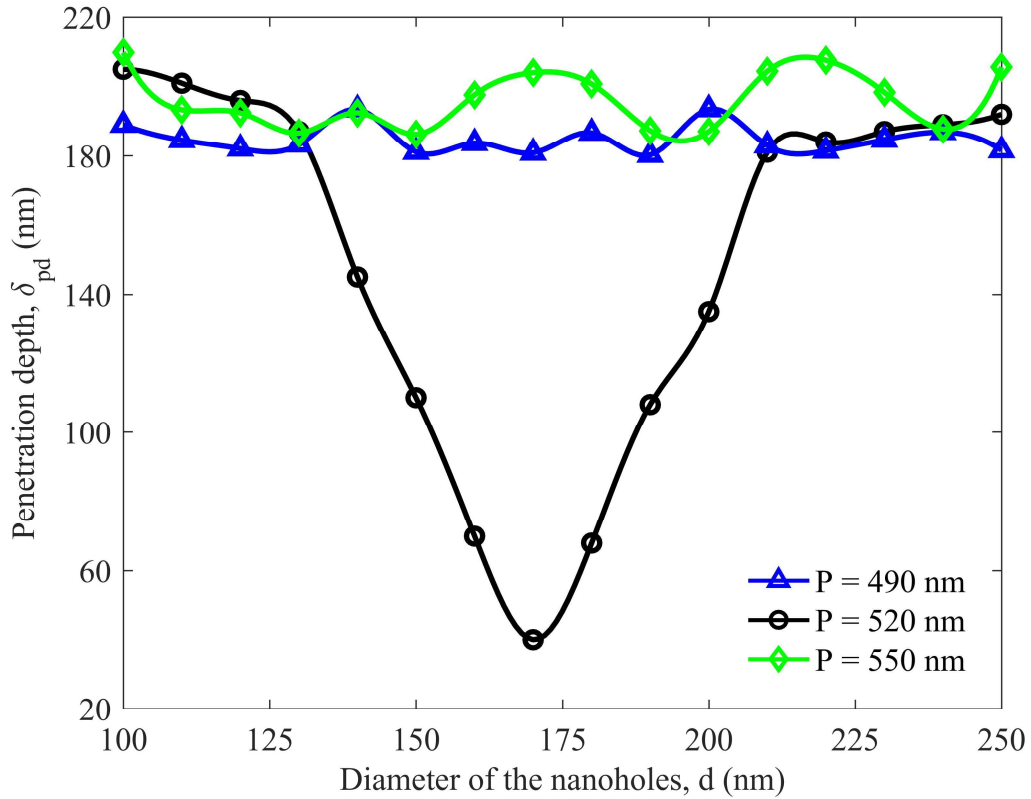


Figure 4.7: Penetration depth (δ_{pd}) vs nanohole diameter, d (nm) for different periodicity of nanoholes. Blue triangle, black circle, and green square represent the penetration depth of the proposed structure for a periodicity of 490, 520, and 550 nm, respectively.

In Figure 4.7, the black circled graph represents the relationship between penetration depth and nanohole diameter for nanohole periodicity of 520 nm, whereas blue starred and green squared represent nanohole periodicity of 490 and 550 nm, respectively. We note that the penetration depth decreases significantly in the proposed structure. Although there are no significant changes in penetration depth for nanohole periodicity of 490 nm and 550 nm, we find smallest penetration depth for nanoholes diameter size of 170 nm with a periodicity of 520 nm.

4.5 Excitation Field

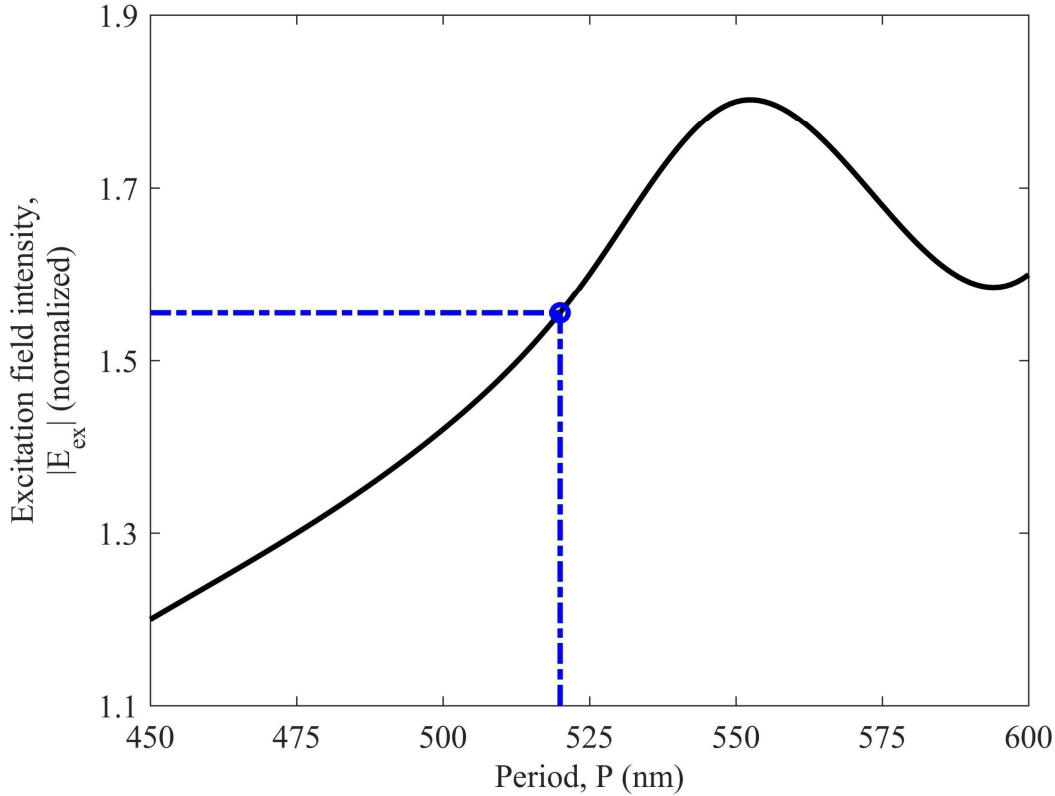


Figure 4.8: Excitation field intensity vs periodicity of nanoholes. The excitation field intensities are normalized by corresponding excitation field intensities of the typical structure. The fields are calculated at a distance of 30 nm from the metal and sample/spacer layer interface. The diameter of the nanoholes is 170 nm. Proposed structure's performance is marked with blue circle.

Excitation field intensity determines how much power the fluorescent will radiate. As we want as much power as possible to be coupled to the detection side, it is important that the fluorescent radiates greater power. Most of the power delivered by the fluorescent molecule is usually lost in the metal, some also reflected to the sample side. In Figure 4.8, we show the relationship between excitation field intensity and period of the nanoholes for a constant nanohole diameter size of 170 nm. We achieve a maximum value of around 1.8 times of that of the typical structure for a period of 750 nm. Although there is an 80 percent improvement in excitation field the penetration depth for 750 nm is around 200 nm, which is not small enough to image single molecule. So, we need a trade-off here. Our first priority is imaging single molecule, improving other detection aiding features are bonus. As we find our minimum detection volume for a period of 520 nm, we mark that point in the graph with a blue circle. We find the improvement to be 56 percent compared to

that of the typical structure. Though we are not availing highest possible improvement in coupled power, we are still getting sufficient improvement with the smallest detection volume possible.

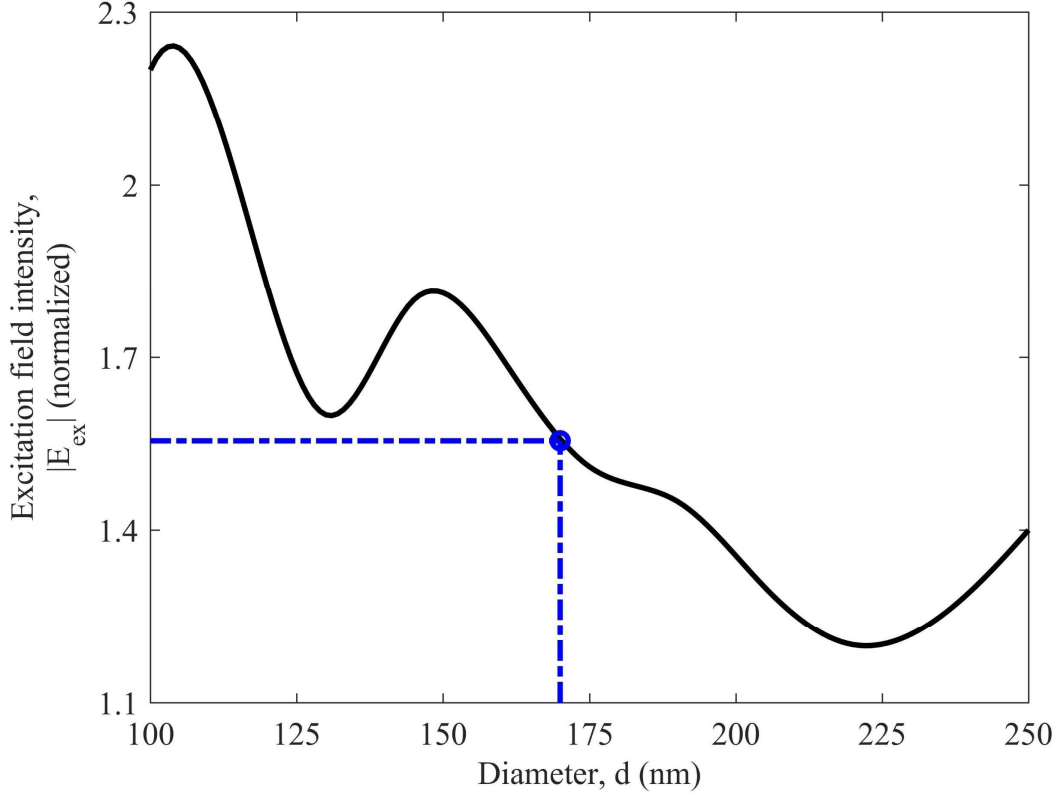


Figure 4.9: Excitation field intensity vs diameter of nanoholes. The excitation field intensities are normalized by corresponding excitation field intensities of the typical structure. The fields are calculated at a distance of 30 nm from the metal and sample/spacer layer interface. The periodicity of the nanoholes is 520 nm. Performance of the proposed structure is marked with blue circle.

In Figure 4.9, we show the relationship between excitation field intensity and diameter of the nanoholes for a constant periodicity of 520 nm. We achieve a maximum of 2.25 times of that of the typical structure when the diameter of the nanoholes is around 110 nm. However, same trade-off applies here. For 110 nm diameter size, we achieve a detection volume of around 200 nm, which is not sufficiently small to image single molecule that is the primary objective of this thesis. So, we mark the improvement for our proposed structure with a blue circle, and find the improvement to be 56 percent, which we already know from previous discussion.

4.6 Power Coupled to Detection Side

Another most important detection feature is the amount of power coupled to the detection side (where the glass prism is). We monitor the near field from the FDTD simulation. After a complete simulation, we project this near field data to far field. Finally, we use the far field to calculate the power coupled to detection side.

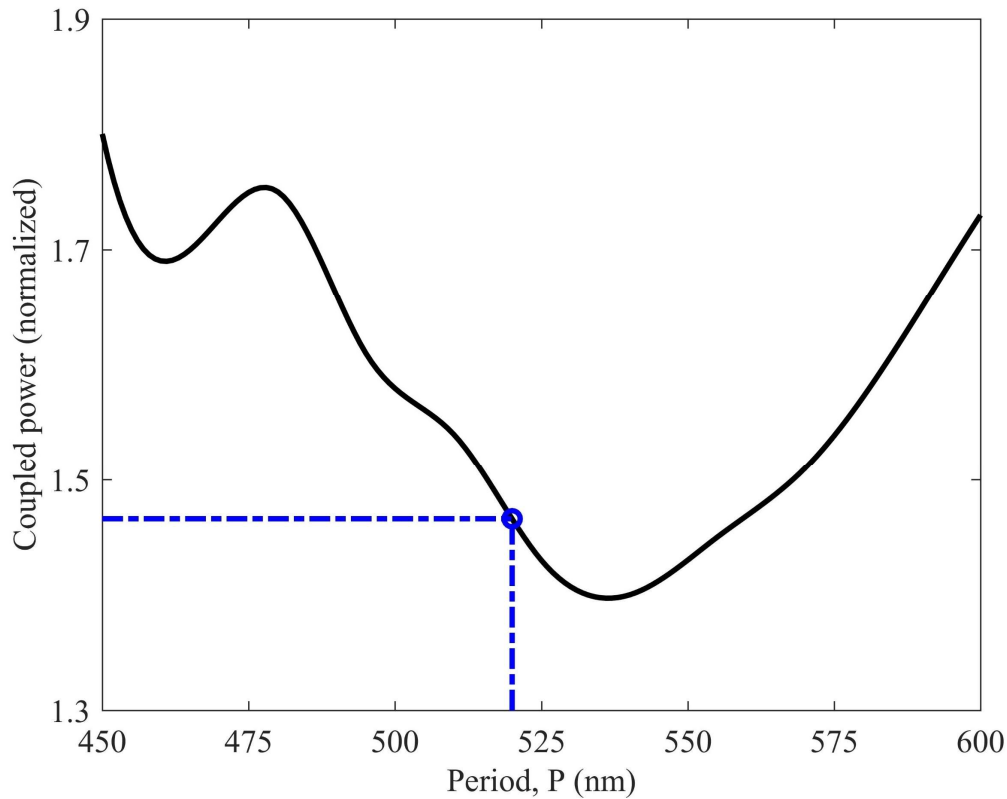


Figure 4.10: Power coupled to detection side as a function of periodicity of the nanoholes. Coupled power is normalized by the corresponding coupled power of the typical structure. Coupled power is calculated by integrating the far-field at a distance of 1 m that is generated by projecting near field to far field. The diameter of the nanoholes is 170 nm. Performance of the proposed structure is marked with blue circle.

In Figure 4.10, we show the relationship between the coupled power and the period of the nanoholes for a constant nanohole diameter of 170 nm. We achieve maximum coupled power of 1.8 times of that of the typical structure for a periodicity of 450 nm, whereas our proposed structure's improvement is 1.47 times, marked with blue circle in Figure 4.10. Forty seven percent

improvement in coupled power, along with a detection volume of 40 nm, is excellent for imaging single molecule, rather having 80 percent improvement in coupled power with almost no improvement in detection volume, which is around 200 nm.

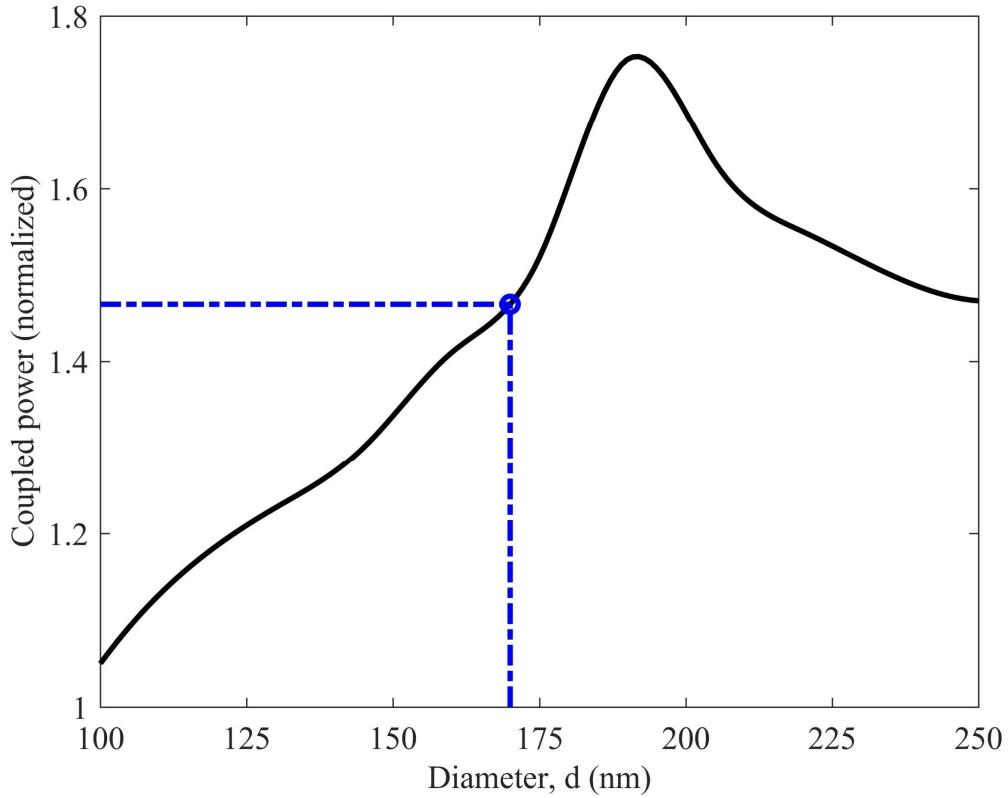


Figure 4.11: Power coupled to detection side as a function of the diameter of the nanoholes. Coupled power is normalized by the corresponding coupled power of the typical structure. Coupled power is calculated by integrating the far-field at a distance of 1 m that is generated by projecting near field to far field. The period of the nanoholes is 520 nm. Performance of the proposed structure is marked with blue circle.

In Figure 4.11, we show how coupled power changes when nanohole diameter changes for a nanohole period of 520 nm. Here, we achieve maximum improvement of around 75 percent in coupled power for nanohole diameter of 190 nm. However, this diameter size offers a detection volume of Performance of the proposed structure is marked with blue circle in Figure 4.11. The proposed structure offers improvement of 47 percent, which is more satisfactory because the proposed structure guarantees minimum detection volume.

4.7 Peak SPCE Intensity

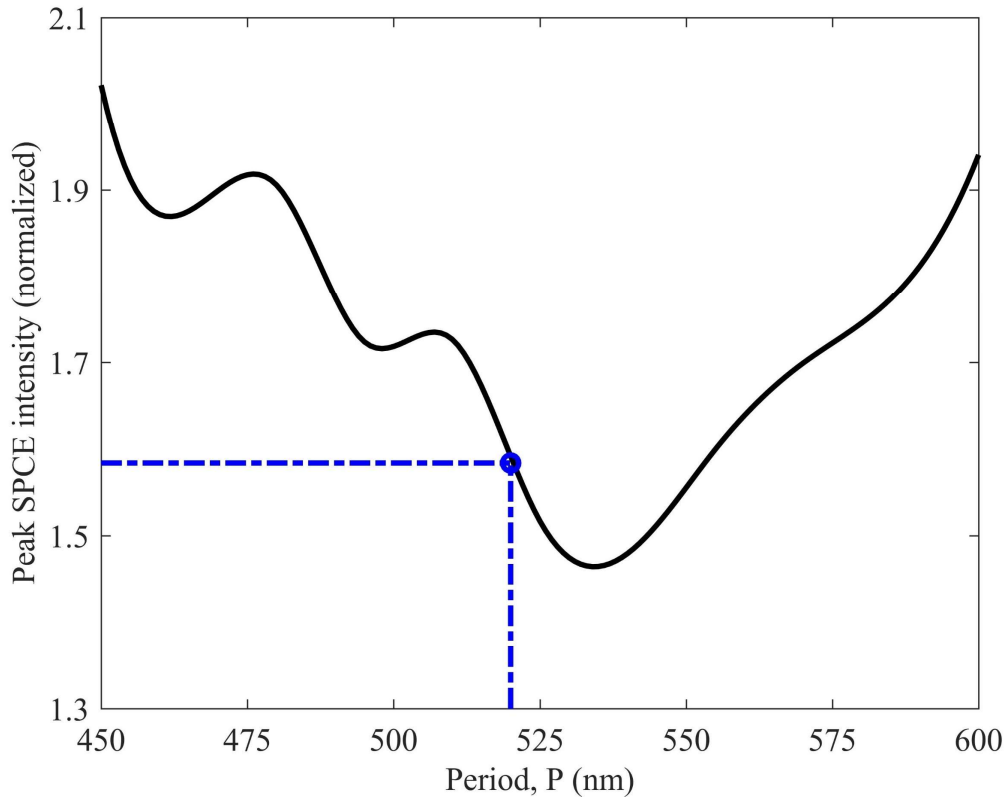


Figure 4.12: Peak SPCE intensity vs period of the nanoholes. The maximum emitted electric field intensity at the detection side is named as peak SPCE intensity. Peak SPCE intensity is normalized by the corresponding peak SPCE intensity of the typical structure. The diameter of the nanoholes is 170 nm. Performance of the proposed structure is marked with blue circle.

Far field radiation pattern shows highly directional emission of light, we calculate the maximum field intensity in the far field. We denote this maximum far field intensity as peak SPCE intensity. In Figure 4.12, we show the relationship between peak SPCE intensity and period of the nanostructures for a constant nanometer diameter of 170 nm. We achieve highest peak SPCE intensity of 2 times of that of the typical structure for a periodicity of 450 nm, whereas our proposed structure's improvement is 1.58 times, marked with blue circle in Figure 4.12. Forty seven percent improvement in coupled power, along with a detection volume of 40 nm, is great for imaging single molecule, rather having 100 percent improvement in peak SPCE with almost no improvement in detection volume, which is around 200 nm.

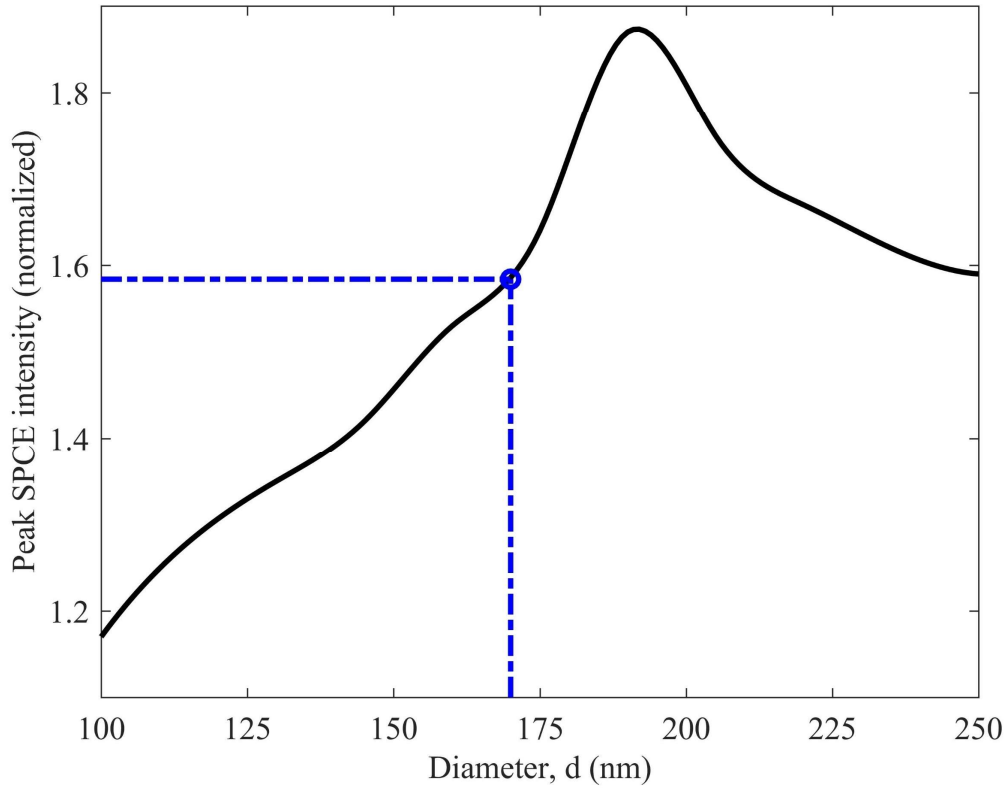


Figure 4.13: Peak SPCE intensity vs diameter of the nanoholes. The maximum emitted electric field intensity at the detection side is named as peak SPCE intensity. Peak SPCE intensity is normalized by the corresponding peak SPCE intensity of the typical structure. The period of the nanoholes is 520 nm. Performance of the proposed structure is marked with blue circle.

In Figure 4.13, we show how peak SPCE intensity depends on the diameter of the nanoholes when nanohole period is 520 nm. We find a maximum improvement of 85 percent when diameter is around 190 nm. However, it is still not desired as we get very little improvement in detection volume for this nanometer diameter. Improvement offered by our proposed structure is 58 percent, and it is a great achievement considering the fact that proposed structure offers minimum detection volume.

4.8 Comprehensive Performance Analysis

Performance of the proposed structure ($P = 520$ nm and $d = 170$ nm) is listed in Table 4.1, and compared with that of the typical structure.

Table 4.1: Performance comparison between typical and proposed structure

| Property | Typical Structure | Proposed Structure | Comments |
|--------------------------------|--------------------------|---------------------------|-----------------------------------|
| Penetration depth | 250 nm | 40 nm | 84% reduction in detection volume |
| Excitation field intensity | 1 | 1.56 | 56% improvement |
| Normalized coupled power | 1 | 1.47 | 47% improvement |
| Normalized peak SPCE intensity | 1 | 1.58 | 58% improvement |

For better visual understanding, we plot a bar chart in Figure 4.14. From this bar chart, we find the detection volume of the proposed structure is only 16 percent compared to the typical detection volume. This reduction of detection volume is significant in imaging single molecule with SPCE based sensing.

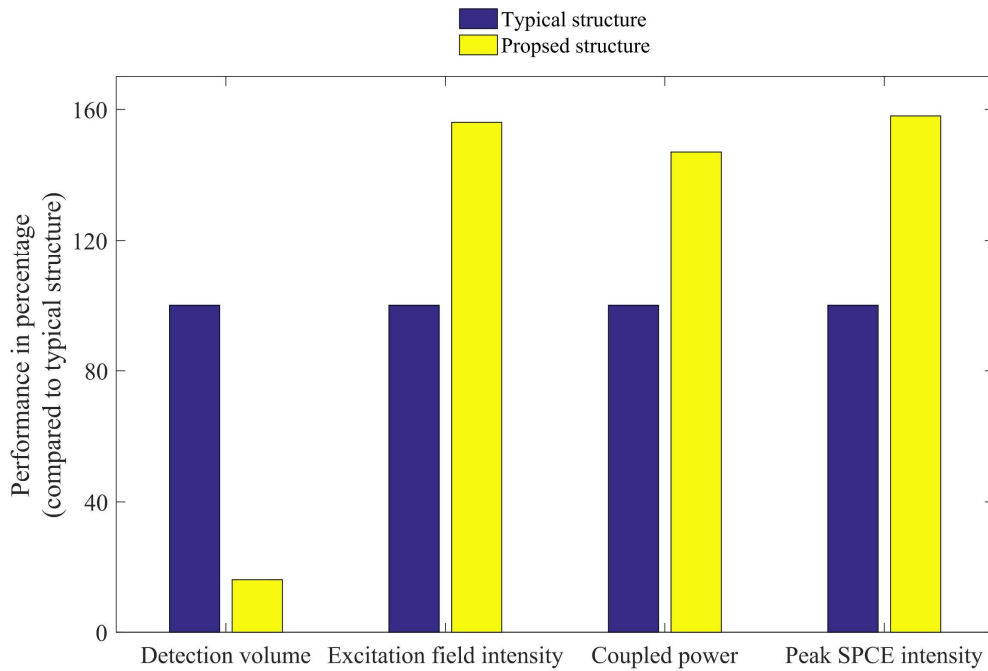


Figure 4.14: Bar chart of performance of proposed structure compared with typical structure. The performances are expressed in percentage of that of the typical structure. Blue bars correspond to the typical structure whereas yellow bars correspond to the proposed structure.

Performance of other possible candidates are also discussed below. If we consider a structure that provides maximum excitation field intensity, then we pick the combination of $P = 520$ nm and $d = 110$ nm. We call it candidate 1 structure. Again, if we consider a structure that offers maximum power coupled to detection side, then we pick a combination of $P = 450$ nm and $d = 170$ nm. And we call this structure candidate 2. Comparison of the proposed structure with typical and candidate structures is shown in Table 4.2.

Table 4.2: Comparison of proposed structure with typical and other candidate structures

| Property | Typical Structure | Proposed Structure P=520 nm d=170 nm | Candidate 1 P=520 nm d=110 nm | Candidate 2 P=450 nm d=170 nm |
|--------------------------------|--------------------------|---|--|--|
| Penetration depth | 250 nm | 40 nm | 200 nm | 180 nm |
| Excitation field intensity | 1 | 1.56 | 2.25 | 1.2 |
| Normalized coupled power | 1 | 1.47 | 1.15 | 2 |
| Normalized peak SPCE intensity | 1 | 1.58 | 1.2 | 2 |

We also plot a bar chart, shown in Figure 4.15, which gives a comprehensive overview of the performances of different structures.

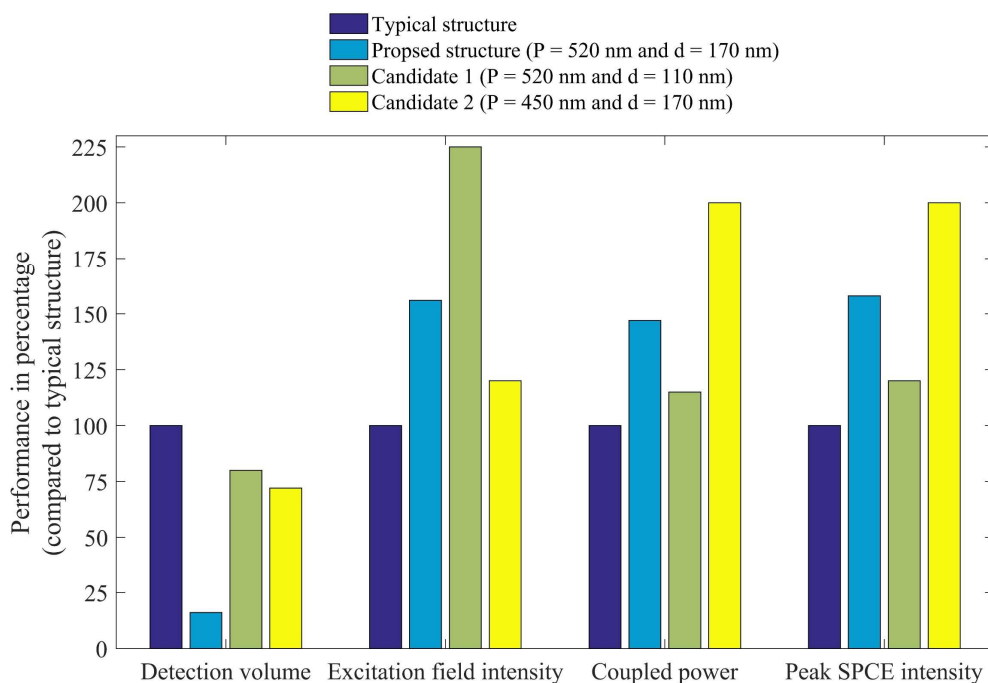


Figure 4.15: Comparison of the performances of different structures. The dark blue, light blue, green, and yellow bars represent the typical, proposed, candidate 1, and candidate 2 structure, respectively.

In Figure 4.15, we see that the detection volume is significantly smaller than other structures, and only the proposed structure is capable of imaging single molecule. Candidate 1 structure offers the highest excitation field intensity, but improvement in power coupled to detection side very negligible. Similarly, although candidate 2 offers great improvement in power coupled to detection side, it offers little improvement in excitation field intensity. On the other hand, proposed structure offers smallest detection volume, along with significant improvement in both excitation field intensity and power coupled to detection side.

4.9 Theoretical Explanation

Metal layer with nanohole structures behaves drastically differently for different wavelengths[37]. There are several modes for a specific nanohole diameter and periodicity. As we vary the nanohole diameter and periodicity, we actually vary the modes, i.e. resonating wavelengths. For a particular combination of nanohole diameter size and periodicity it resonates at both fluorophore's excitation and emission wavelengths. We exploit this feature. As the structure resonates at excitation

wavelength of Rhodamine B, we find great improvement in excitation field intensity and also the field is tightly bound that means a smaller detection volume. On the other hand, when the structure resonates at emission wavelength of the fluorophore, it results in significantly higher power coupled to detection side. One more interesting thing is that the power coupled to detection side and the peak SPCE intensity graphs have similar shape, which means that most of the power is being emitted through the emission angle, which ensures high directionality of the emission that is very important in detection mechanism.

Chapter 5

Conclusion and Future Works

Surface plasmon coupled emission (SPCE) is over all an appropriate method for biodetection. SPCE is advantageous compared to conventional detection schemes because of several aspects including high directionality of fluorescence emission, reduced photobleaching, reduction of background noise, high spectral resolution due to strong wavelength dependent angular emission, study of surface attached fluorophores, etc.

The major drawback to image single molecule with SPCE is large detection volume. Other drawbacks include low power coupling to detection side. The aim of this thesis is to design a nanostructure so that it provides sufficiently small detection volume, which is capable of imaging single molecule. Our proposed structure replaces the metal layer with nanostructured metal that contains periodic nanoholes. We achieve the followings:

- We designed a nanostructure that has two design features: diameter and period of the nanoholes.
- We found the best combination of nanohole diameter size and periodicity so that it offers minimum detection volume (40 nm penetration depth only).
- We compared the proposed structure with state-of-the-art structure and other candidate structures, and it outperformed all of them in imaging single molecule.
- The proposed structure also significantly improves excitation field intensity and power coupled to detection side.

Our proposed structure has some limitations too. As the performance of the structure is strongly dependent on the diameter and period of the nanoholes, its performance is highly dependent on fabrication processes. Fabrication processes result in various irregularities, such as unequal diameter size and/or periodicity, which results in degraded performance. Thus, the improvement we reported is the highest possible performance improvement with such structure, whereas the actual performance will have a strong correlation with the fabrication processes.

5.1 Future Work

In the future, we plan to experimentally verify our simulation results. The experimental verification of detection volume reduction and performance improvement will certainly address practical issues and will add great value to our work. Also, we may modify the highly polarized emission by using anisotropic materials and measure the Kerr effect on the emission.

Bibliography

- [1] L. Polerecký, J. Hamrle, and B. D. MacCraith, "Theory of the radiation of dipoles placed within a multilayer system," *Appl. Opt.*, vol. 39, no. 22, p. 3968, 2000.
- [2] R. E. Benner, R. Dornhaus, and R. K. Chang, "Angular emission profiles of dye molecules excited by surface plasmon waves at a metal surface," *Opt. Commun.*, vol. 30, no. 2, pp. 145–149, 1979.
- [3] J. Enderlein, "A theoretical investigation of single-molecule fluorescence detection on thin metallic layers," *Biophys. J.*, vol. 78, no. 4, pp. 2151–2158, 2000.
- [4] J. Enderlein, "Single-molecule fluorescence near a metal layer," *Chem. Phys.*, vol. 247, no. 1, pp. 1–9, 1999.
- [5] J. Enderlein and T. Ruckstuhl, "The efficiency of surface-plasmon coupled emission for sensitive fluorescence detection.," *Opt. Express*, vol. 13, no. 22, pp. 8855–8865, 2005.
- [6] Z. Gryczynski, J. Borejdo, N. Calander, E. G. Matveeva, and I. Gryczynski, "Minimization of detection volume by surface-plasmon-coupled emission," *Anal. Biochem.*, vol. 356, no. 1, pp. 125–131, 2006.
- [7] J. R. Lakowicz, "Radiative decay engineering 4. Experimental studies of surface plasmon-coupled directional emission," *Anal. Biochem.*, vol. 324, no. 2, pp. 153–169, 2004.
- [8] I. Gryczynski, J. Malicka, K. Nowaczyk, Z. Gryczynski, and J. R. Lakowicz, "Effects of Sample Thickness on the Optical Properties of Surface Plasmon-Coupled Emission," *J. Phys. Chem. B*, vol. 108, no. 32, pp. 12073–12083, 2004.
- [9] T. Neal, K. Okamoto, and A. Scherer, "Surface plasmon enhanced emission from dye doped polymer layers.," *Opt. Express*, vol. 13, no. 14, pp. 5522–5527, 2005.
- [10] J. Enderlein, T. Ruckstuhl, and S. Seeger, "Highly efficient optical detection of surface-generated fluorescence," *Appl. Opt.*, vol. 38, no. 4, p. 724, 1999.
- [11] I. Gryczynski, J. Malicka, Z. Gryczynski, K. Nowaczyk, and J. R. Lakowicz, "Radiative decay engineering 4. Experimental studies of surface plasmon-coupled directional emission," *Anal. Chem.*, vol. 76, no. 14, pp. 4076–4081, 2004.
- [12] N. Calander, "Theory and Simulation of Surface Plasmon-Coupled Directional Emission from Fluorophores at Planar Structures," *Anal. Chem.*, vol. 76, no. 8, pp. 2168–2173, 2004.
- [13] N. Calander, "Surface plasmon-coupled emission and fabry - Perot resonance in the sample layer: A theoretical approach," *J. Phys. Chem. B*, vol. 109, no. 29, pp. 13957–13963, 2005.
- [14] Z. Gryczynski, I. Gryczynski, E. G. Matveeva, N. Calander, R. Grygorczyk, I. Akopova, S.

- Bharill, P. Muthu, S. Klidgar, and J. Borejdo, "New Surface Plasmons Approach to Single Molecule Detection (SMD) and Fluorescence Correlation Spectroscopy (FCS).," *Proc SPIE*, vol. 6444, p. 64440G, 2007.
- [15] D. S. Smith, Y. Kostov, and G. Rao, "Signal enhancement of surface plasmon-coupled directional emission by a conical mirror.," *Appl. Opt.*, vol. 47, no. 28, pp. 5229–5234, 2008.
- [16] S. Venkatesh, P. K. Badiya, and S. S. Ramamurthy, "Low-dimensional carbon spacers in surface plasmon-coupled emission with femtomolar sensitivity and 1000-fold fluorescence enhancements," *Chem. Commun.*, vol. 51, no. 37, pp. 7809–7811, 2015.
- [17] J. Borejdo, Z. Gryczynski, N. Calander, P. Muthu, and I. Gryczynski, "Application of surface plasmon coupled emission to study of muscle," *Biophys. J.*, vol. 91, no. 7, pp. 2626–2635, 2006.
- [18] E. Matveeva, J. Malicka, I. Gryczynski, Z. Gryczynski, and J. R. Lakowicz, "Multi-wavelength immunoassays using surface plasmon-coupled emission," *Biochem. Biophys. Res. Commun.*, vol. 313, no. 3, pp. 721–726, 2004.
- [19] J. R. Lakowicz, *Principles of fluorescence spectroscopy*. Springer Science & Business Media, 2007.
- [20] B. Valeur and M. Nuno, *Molecular fluorescence: principles and applications*. John Wiley & Sons, 2012.
- [21] J. R. Lakowicz, "Radiative decay engineering 3. Surface plasmon-coupled directional emission," *Anal. Biochem.*, vol. 324, no. 2, pp. 153–169, 2004.
- [22] K. Ray, H. Szmazinski, J. Enderlein, and J. R. Lakowicz, "Distance dependence of surface plasmon-coupled emission observed using Langmuir-Blodgett films," *Appl. Phys. Lett.*, vol. 90, no. 25, 2007.
- [23] C. C. Katsidis and D. I. Siapkas, "Systems With Coherent , Partially Coherent , and Incoherent Interference," *Appl. Opt.*, vol. 41, no. 19, pp. 3978–3987, 2002.
- [24] David K. CHENG, *Field and Wave Electromagnetics*, Volume 2. New York: Addison-wesley, 1989.
- [25] E. D. Palik, *Handbook of optical constants of solids*, Volume 2. Academic press, 1998.
- [26] G. M. Hale and M. R. Querry, "Optical Constants of Water in the 200-nm to 200-microm Wavelength Region.," *Appl. Opt.*, vol. 12, no. 3, pp. 555–563, 1973.
- [27] S. Kedenburg, M. Vieweg, T. Gissibl, and H. Giessen, "Linear refractive index and absorption measurements of nonlinear optical liquids in the visible and near-infrared spectral region," vol. 25240, no. 2010, pp. 6230–6240, 2012.
- [28] "AAT Bioquest's interactive Spectrum Viewer," 2018. [Online]. Available:

https://www.aatbio.com/spectrum/Rhodamine_B.

- [29] J. P. Berenger, “A perfectly matched layer for the absorption of electromagnetic waves,” *J. Comput. Phys.*, vol. 114, pp. 185–200, 1994.
- [30] E. Betzig, E. Betzig, R. J. Chichester, and R. J. Chichester, “Single Molecules Observed by Near-Field Scanning Optical Microscopy,” *Science (80-.)*, vol. 262, no. 5138, pp. 1422–1425, 1993.
- [31] J. R. Lakowicz, “Radiative decay engineering 5: Metal-enhanced fluorescence and plasmon emission,” *Anal. Biochem.*, vol. 337, no. 2, pp. 171–194, 2005.
- [32] E. Fort and S. Grésillon, “Surface enhanced fluorescence,” *J. Phys. D. Appl. Phys.*, vol. 41, no. 1, 2008.
- [33] M. H. Chowdhury, K. Ray, C. D. Geddes, and J. R. Lakowicz, “Use of silver nanoparticles to enhance surface plasmon-coupled emission (SPCE),” *Chem. Phys. Lett.*, vol. 452, no. 1–3, pp. 162–167, 2008.
- [34] J. S. Yuk, B. D. MacCraith, and C. McDonagh, “Signal enhancement of surface plasmon-coupled emission (SPCE) with the evanescent field of surface plasmons on a bimetallic paraboloid biochip,” *Biosens. Bioelectron.*, vol. 26, no. 7, pp. 3213–3218, 2011.
- [35] S. Rauf, M. J. A. Shiddiky, A. Asthana, and K. Dimitrov, “Fabrication and characterization of gold nanohole electrode arrays,” *Sensors Actuators, B Chem.*, vol. 173, pp. 491–496, 2012.
- [36] E. N. Economou, “Surface plasmons in thin films,” *Phys. Rev.*, vol. 182, no. 2, pp. 539–554, 1969.
- [37] L. Wu, P. Bai, X. Zhou, and E. P. Li, “Reflection and transmission modes in nanohole-array-based plasmonic sensors,” *IEEE Photonics J.*, vol. 4, no. 1, pp. 26–33, 2012.